December 2017

PhD Dissertation

Automated Methods for Analysis of Three-Dimensional Morphology and Dynamics in Living Cells With a Label-Free Digital Holographic Microscope

Graduate School of Chosun University

Department of Computer Engineering

Keyvan Jaferzadeh Khorramabadian

라벨이없는 디지털 홀로 그래픽 현미경으로 살아있는 세포의 3 차원 형태와 역 동성을 분석하는 자동화 된 방법

2017 년 10 월 10 일

조선대학교 대학원

컴 퓨 터 공 학 과

케이반

Automated Methods for Analysis of Three-Dimensional Morphology and Dynamics in Living Cells With a Label-Free Digital Holographic Microscope

Advisor: Professor Shin Seok-Joo

This Thesis is submitted to the Graduate School of Chosun University in partial fulfillment of the requirements for the award of a PhD degree

2017 년 10 월

Graduate School of Chosun University

Department of Computer Engineering

Keyvan Jaferzadeh Khorramabadian

This certifies that the degree of Doctor of Philosophy of Keyvan Jaferzadeh Khorramabadian is approved by:

권구락 (chair of the committee)

문인규(committee member)

강문수(committee member)

이충규(committee member)

신석주(committee member)

Graduate School of Chosun University

Table of Contents

List of Tables

List of Figures

Abbreviations

RBC: Red Blood Cell

DHM: Digital Holographic Microscopy

CPU: Central Processing Unit

GPU: Graphics Processing Unit

DSP: Digital Signal Processing

FFT: Fast Fourier Transform

2D: 2-dimensional

3D: 3-dimensional

MCH: Mean Corpuscular Hemoglobin

MCHSD: Mean Corpuscular Hemoglobin Surface Density

MCV: Mean Corpuscular Volume

SA: Surface Area

SA/V: Surface Area to Volume Ratio

PRNN: Pattern Recognition Neural Network

QPM: Quantitative Phase Microscopy

Abstract

Automated Methods for Analysis of Three-Dimensional Morphology and Dynamics in Living Cells with a Label-Free Digital Holographic Microscope

By: Keyvan Jaferzadeh Khorramabadian

Advisor: Shin Seok-Joo

Department of Computer Engineering

Graduate School of Chosun University

The most common type of microscope is the optical two-dimensional (2D) microscope. This is an optical device containing one or more lenses producing an enlarged image of a sample placed in the focal plane of the first lens. Optical microscopes have refractive glass and occasionally of plastic or quartz, to focus light into the eye or another light detector. The usage of the light microscopes has been around and will be. However, there is a big flaw in using 2D microscopes. This microscopic system suffers from losses of quantitative detailed information about 3rd dimension (thickness) of transparent or semitransparent microscopic samples. The problem is not limited only to this one. There are cases in which samples are transparent or semi-transparent. In these cases the light can not be reflected thus a high contrast image will not be produced. This can falsify cell studies and results to incorrect outputs. To overcome these problems, three-dimensional imaging techniques are suggested. Among these techniques, digital holographic microscopy (DHM) has been successfully applied in a range of application areas. Indeed, DHM is not destructive for specimens and sample can be investigated many times and by any other optical methods while the electron microscopy methods are destructive. Another advantage of using DHM is that we can investigate the cells in single-cell level. Moreover, quantitative phase image obtained by DHM enables one to measure

characteristic properties of cells such as thickness, volume, surface area and projected surface area. The usage of DHM can be extended to time-lapse imaging (four dimensional imaging; last dimension is the time). Time lapse imaging enables us to study cell changes or growths in different time stamps and monitor it.

In this dissertation, we would like to address different automated techniques and methods which can enable us to study live cells in non-destructive manner and single-cell level. Several approaches for studying and analyzing live cells are proposed and applied. To do so, two subject cells are concerned. The first cell type is red blood cell (RBC) and the second one is cardiomyocyte. Each type of these cells has different cell structure. In the case of RBC, DHM is perfectly suited for different experiments and it can provide thickness of the cell in nanometer accuracy. The reason is that cell has no nuclei and organelles. So, we are able to study different characteristic of the cell. Cardio cell is well suited for time-lapse studies. The reason is that optical path difference can be measured by DHM device. This can help us studying cell structure changes during different states of beating. Several experimental results are conducted and in some cases results are compared with the chemical experiments to show the feasibility of the proposed methods.

[KEYWORDS]: Human Cell Analysis, Digital Holographic Microscopy, Red Blood Cell, Cardio Cell

1 Introduction

Most of the biological cells, as well as red blood cells or cardiomyocytes, are transparent or semi-transparent thus the amplitude of the light which interacts with them is minimally affected. Different staining methods have been developed that enable cells to absorb light but they cannot solve this issue in general. For example, in some cases different dyes are used in order to enhance the contrast of transparent samples [1] in light-filed microscopy. Dark field microscopy can also be used to image transparent cells [1]. Another thing is that the conventional techniques are unable to provide 3D images or sometime the accuracy is not enough. Also, these methods are invasive and will manipulate the specimen. Confocal laser scanning microscopy can also be used to measure 3d volume of the specimen. Three-dimensional volume image can be built up by stacking the 2D optical sections for a range of specimen planes [1]. Therefore, it is hard to quantitatively examine images of these cells obtained by these microscopy techniques. The search for a method to study cells accurately without labeling or staining them has resulted in several interferometric quantitative microscopy techniques utilizing the phase properties of coherent light to image a sample. One of them is digital holography. In 1948, Dennis Gabor invented a way to encode the phase of the light both as information and as a record containing all the information in a single recording, i.e. the hologram. Holograms are commonly used as pieces of art and are displayed as illuminated 3-D images. Therefore, imaging techniques measuring changes in the phase of light like digital holographic microscopy (DHM) can quantitatively visualize the 3D shape of those cells in non-invasive manner [2-8]. Using DHM it is possible to measure cell shape, volume and dry mass without any labeling and with a very low intensity light source where the intensity is well below what is considered photo-toxic. As it is mentioned above, DHM is not destructive for specimens and it can be investigated once more and by any other optical. Moreover, quantitative phase image obtained by DHM enables one to measure characteristic

properties such as volume, projected surface area, mean corpuscular hemoglobin (MCH) and MCH surface density (MCHSD) of the biological cell specially RBC. Digital holographic microscopy (DHM) is a promising tool for real-time 3D cell imaging owing to its capability for non-invasive visualization and for quantifying transparent biological cells [9-12]. DHM has been utilized in various kinds of cell studies (protozoa, bacteria, plant cells, blood cells, nerve cells, or stem cells)[13-21], and also human red blood cells [22-27], in the absence of labeling.

Since the images are recoded by a CCD camera and holograms are reconstructed by a numerical reconstruction technique [28-30], the output is a digital image. Therefore, lots of image processing techniques can be used to enhance and evaluate quantitative parameters related to cell studies. The techniques should be automated, fast and accurate enough to be used in life science researches. In this dissertation, we would like to focus on studies of live cells and monitor them in an automated manner. Also, results are quantitative thanks to digital holographic microscopy.

Also, two subject samples are studied here. The first one is red blood cells. Red blood cells (RBCs) are composed of water, proteins (the most abundant of which is hemoglobin), lipids, and carbohydrates. Also, RBC contains hemoglobin which binds to either oxygen or carbon dioxide. This allows oxygen to be transported to tissues and organs and carbon dioxide to be taken away during microcirculation. The biconcave shape of the erythrocyte is extremely important in the functionality of RBCs. It allows the membrane to have a high surface area to volume (SA/V) ratio facilitating large reversible elastic deformation of the RBC while squeezing through the tiny capillaries [31-33]. Mature erythrocytes, which are sometimes also referred to as discocytes, are the main cell type in the blood circulation. Their biconcave shape is formed by a flexible membrane that allows significant deformation. This configuration has the maximum surface area for a given volume and allows rapid deformations while passing through small capillaries during microcirculation. Such a biconcave shape is assumed to have resulted from the minimization of the free energy of the membrane under area and volume

constraints, since there are no complex internal structures within an RBC. RBCs must adapt to a wide range of capillary sizes, and deform while maintaining their cellular integrity and function. This is made possible by the absence of a three-dimensional (3D) cytoskeleton in RBCs. Their shape and mechanical integrity are maintained instead by a two-dimensional (2D) hexagonal lattice formed of flexible spectrin tetramers, which are linked by actin oligomers. Since the side length of actin (70-80 nm) is much smaller than the contour length of a spectrin tetramer (approximately 200 nm), it is believed that spectrins are the principal contributors to the bending of membranes or curvature modulus [33, 34]. Accordingly, it has drawn considerable attentions into the pathology research in the clinical relevant blood diseases. Pathological disorders can modify RBCs and lead to significant alterations in its original shape [34]. The consequences of modified RBC often are observed as clinical symptoms ranges from obstruction of capillaries and restriction of blood flow to tissues to necrosis and organ critical damages [34-39]. Also, counting cell types in the blood sample is another important task for investigating clinical status which can be evaluated by well-known methods such as complete blood count (CBC) or RBC distribution width (RDW) which are part of cytometry field. Because an automated cell counter samples and counts so many cells, the results are reliable in most of the cases [40]. However, certain abnormal cells in the blood may not be identified correctly, requiring manual review and identification of any abnormal RBCs the instrument could not categorize. This information can be very helpful regarding identifying the cause of a patient's anemia. Abnormal increases or decreases in RBC counts as revealed in a complete RBC count may indicate that you have an underlying medical condition that calls for further evaluation.

The second study subject is cardiac muscle cells or cardiomyocytes or so-called myocardiocytes. There are two types of cells within the heart: the cardiomyocytes and the cardiac pacemaker cells. Cardiomyocytes make up the atria which is the chambers blood enters the heart and the ventricles where blood is collected and pumped out of the heart. These

cells must be able to shorten and lengthen their fibers and the fibers must be flexible enough to stretch. The primary function of the heart is to pump blood efficiently by virtue of an orchestrated contraction–relaxation cycle of the working cardio muscles. The human heart contains an estimated 2 to 3 billion cardiomyocytes cells. By coordinated contraction, these cells control blood flow through the blood vessels of the circulatory system. During the cardiomyocyte contraction, the whole cell changes its 3D shape rapidly, with meaningful intermediate events taking place on the short intervals (milliseconds) [41]. Also, the beating attributes such as beating frequency and peak changes are related to the cellular response to various stimuli and also to differentiation/maturation status. Cardiomyocytes respond to drugs and naturally occurring hormones and it alters the heart-beat rate. Drug development requires the testing of new chemical entities for adverse effects. Adverse drug side effects, such as cardiotoxicity is a major concern in drug development and a major cause of drug withdrawal from the market [42]. Therefore, safety assessments should be performed during drug development to see the possible side effects of the drug; especially those ones which interfere with the well-choreographed and elaborate movement of ions across cardiomyocytes membrane disrupting the electrical activity and beating of the heart [43]. Accordingly, pharmaceutical companies and researchers should ensure that the effects of lead candidate compounds on cardiac function strictly satisfy safety criteria. Therefore, it is highly important to establish more quantitative examination during drug developments and its effects on cardiomyocytes in vitro using data analysis algorithms for preventing late stage failure [42].

A. Motivations

As it has been mentioned previously, most of the biological cells are transparent or semi-transparent thus the amplitude of the light which interacts with them is minimally affected. Therefore, only amplitude recording cannot help in studying different aspects of these cells.

Also, it is hard to quantitatively examine images of these cells obtained by the conventional microscopy techniques.

By the invention of Gabor holograms in 1984 a new way to encode the phase of the light both as information and as a record containing all the information in a single recording hologram was introduced. Thus, these holograms can be used to study transparent or semitransparent human and animal living cells. Also, digital holographic microscopy (DHM) can quantitatively visualize the 3D shape of those cells in non-invasive manner. Using DHM it is possible to measure cell shape, volume and dry mass without any labeling and with a very low intensity light source where the intensity is well below what is considered photo-toxic. As it is mentioned above, DHM is not destructive for specimens and it can be investigated again and by any other optical technique. When we need to observe fine changes occurring in sensitive cells, any intervention (washing step, addition of a label, high light intensity imaging, etc.) strongly alter their natural state and can lead to falsify results. DHM can preserve the cell natural state and thus offer physiologically relevant measurement.

Moreover, quantitative phase image obtained by DHM enables one to measure characteristic properties such as volume, projected surface area, mean corpuscular hemoglobin (MCH) and MCH surface density (MCHSD) of the biological cell specially RBC. Digital holographic microscopy (DHM) is a promising tool for real-time 3D cell imaging owing to its capability for non-invasive visualization and for quantifying transparent biological cells [9-12]. DHM has been utilized in various kinds of cell studies (protozoa, bacteria, plant cells, blood cells, nerve cells, or stem cells)[13-21], and also human red blood cells [22-27], in the absence of labeling. Overall, the motivations can be listed as below:

1- DHM can provide a new method to study transparent or semitransparent cells since it uses phase shift rather than amplitude changes.
2- It is non-invasive thus cells can be study in a safe manner.
3- It is a label-free mean thus cells are not treated by dyes.
4- The laser source is weak so cells cannot be damaged.

5- It can provide 3-dimensional shape of cells for insight investigation.
6- It can be used as a method for time-lapse imaging (4D- imaging).

B. Objectives of Research

The objectives of this research are to find automated methods for analyzing 3-dimensional morphological changes of human RBC and heart muscle cells. Also, monitoring the cell changes in different times, for example dynamic and fluctuations as a function of time.

The objectives can be listed as:

- To study automated method of RBC analysis.
- To study different aspect of RBC like volume, shape and surface area changes in different time.
- To propose new techniques for RBC classification according to the abilities of DHM.
- To measure different changes in RBC as a function of time (day changes).
- To study effects of different antiarrhythmic drugs on cardio cells.

C. Organization of the Research

The organization of this thesis is as follows. Chapter 2 gives an overview of digital holographic microscopy method. Chapter.3 will discuss studying of red blood cell and different automated techniques that can be helpful for RBC analysis. Chapter 4 discusses the automated technique to study heart muscle cells in normal cells and drug treated samples. Chapter 5 provides concluding remarks and future research opportunities.

2 Digital Holographic Microscopy

Microscopy is one of the main research and application areas of digital holography. Direct access to the phase as well as amplitude profiles makes quantitative phase microscopy by digital holography (DH-QPM) particularly powerful and versatile. Digital holographic and interferometric principles are the basis of many other techniques of QPM with novel capabilities. The story of holography started by the Gabor when he invented a new microscopic technique [44-46]. His holograms suffer from the problem of twin image. In 1965, a successful holographic microscope was demonstrated by E. Leith and J. Upatnieks. However, the use of holographic microscopy is limited by its inconvenient chemical developing procedures. This drawback is apparently disappearing in the era of digital holography. In DHM, some effort must be made to achieve micrometer or sub-micrometer resolution [47].

Figure 6.1 depicts the setup of a typical transmission-type microscope-based digital holographic microscope. The mirror (M) in the reference arm can be tilted for off-axis holographic recording, or can be movable for phase-shifting recordings. In the specimen arm, a microscope objective (MO) is used to produce a magnified image of the specimen. The digital holographic recording geometry can also be realized as a reflection-type setup, as shown in Fig. 6.2. In the reflection type setup, the object light is back-scattered to provide the object field to the CCD. Because the MO is in the path of the back-scattered object field, lens L is used additionally to provide uniform illumination of the specimen.

DHM is a full field imaging of the phase of the light incident on the sensor. It can be used to image solid samples in reflection, or, which is most common in the case of biological samples, to image transparent samples in transmittance. The most commonly used system for

DHM today uses an optical setup common to that of a Mach-Zender interferometer, but with the reference light at a slight angle to the light passing through the sample, and the image calculation is then performed using a Fresnel approximation. The outcome of the reconstruction of a digital hologram is two images, one representing the amplitude of the light and one representing the phase changes of the light. The amplitude image is similar to an image of the sample captured in ordinary white light. The resolution in the direction of the incident light is very high, down to the order of nanometers. By combining the phase imaging technique with physical rotation of the sample, a high resolution, label-free tomographic image can be obtained. One of the advantages of DHM is that the object that is studied will always be in focus, and the image can be recalculated many times if necessary to find the best focus. Images can be captured of both single cells and populations, and the images can be presented as traditional cell images as well as 3-D representations. DHM can most likely compete with many of the other methods used today within the area of cell biology and microscopy. The technique is easy to learn and simple to use, it is cheap and gives both qualitative and quantitative results [1, 47].

The coherent laser source with wavelength of $\lambda = 684.5\ nm$ is divided into object and reference beam using beam splitter. The object beam illuminates the specimen and creates the object wave front. A microscope objective collects and magnifies the object wave-front, and the object and reference wave fronts are joined by a beam collector to create the hologram. It should be noted that there is a small tilt angle between the object wave front and reference wave to construct “off-axis” holograms. At the end point interfrograms are recorded by a CCD camera and the data is transmitted to a PC for numerical reconstruction algorithms [My cardio paper].

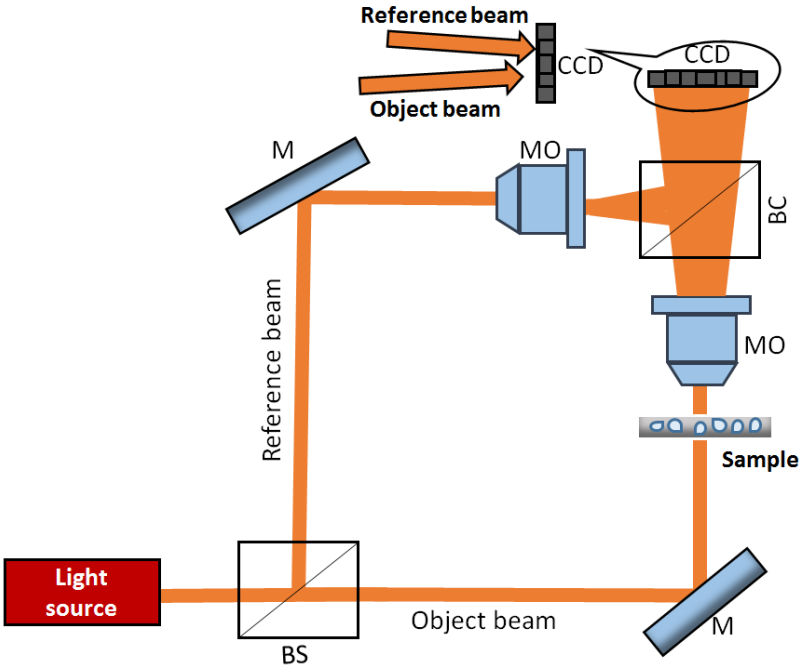

Figure 2.1: A general Presentation of Digital Holographic Microscope

3 Red Blood Cell study by digital holographic microscopy technique:

A typical human red blood cell has a disk diameter of approximately 6.2–8.2 μm and a thickness at the thickest point of 2–2.5 μm and a minimum thickness in the center of 0.8–1 μm, being much smaller than most other human cells. These cells have an average volume of about 90 fL with a surface of about 136 μm2, and can swell up to a sphere shape containing 150 fL, without membrane distension. Adult humans have roughly 20–30 trillion red blood cells at any given time, comprising approximately 70% all cells by number. Women have about 4–5 million red blood cells per microliter (cubic millimeter) of blood and men about 5–6 million; people living at high altitudes with low oxygen tension will have more. Red blood cells are thus much more common than the other blood particles: there are about 4,000–11,000 white blood cells and about 150,000–400,000 platelets per microliter. Human red blood cells take on average 60 seconds to complete one cycle of circulation [48].

RBCs are transparent, thus, they are one of the best case studies for DHM technique. The images or so called holograms (interfrograms) are recorded by a CCD camera and then reconstructed by the numerical reconstruction algorithm. Since the values are the phase shift between sample and surrounding medium, the thickness of the sample can be obtained and quantitative analysis can be conducted. In some analysis phase value is only considered. Throughout this research all the reported values are in either thickness unit or optical path length (OPL). Figure.3.1 shows the recorded hologram, amplitude and phase images. As it can be observed easily, the amplitude image can not reveal the RBC structure easily but phase image shows RBC nicely. It should be noted that phase values should be unwrapped before any further analysis. There are several techniques for unwrapping but we will not explain them in

detail. Also, reconstruction algorithm will be explained below briefly. The focus of this dissertation is to explain different methods and techniques for automatic analysis of RBC and cardiomyocytes.

In off-axis digital holography a small tilt angle is introduced between reference wave and object wave. This small angle can separate virtual image, real image and DC term. By choosing a proper Fourier filter we can filter unwanted zone and have a clear image of the sample. As the digital hologram is recorded, the complex field $\omega_0(x,y)$ at the CCD plane can be retrieved with the Fourier filtering procedures. Subsequently, the complex field at the image plane $\omega_s(x,y)$ can be obtained directly by Fresnel diffraction [47].

$$\omega_s = \exp(-jk0z)\frac{jk0}{2\pi z}\times\exp\left[\frac{-jk0}{2z}\left(x^2+y^2\right)\right] \times \Im\left\{\omega_0(x,y)\exp\left[\frac{-jk0}{2z}\left(x^2+y^2\right)\right]\right\} \tag{1}$$

One of the most important merits of digital holography is that the phase of the sample can be determined quantitatively. This may find important applications in microscopy for biological specimens. We assume that the complex field at the sample plane is $\omega_s=|\omega_s|\exp(j\varphi_s)$), which can be retrieved from a complex hologram obtained by digital holography. Consequently, the phase of ω_s can be obtained by:

$$\varphi_w = \tan^{-1}\left\{\frac{Real(\omega_s)}{Im(\omega_s)}\right\} \tag{2}$$

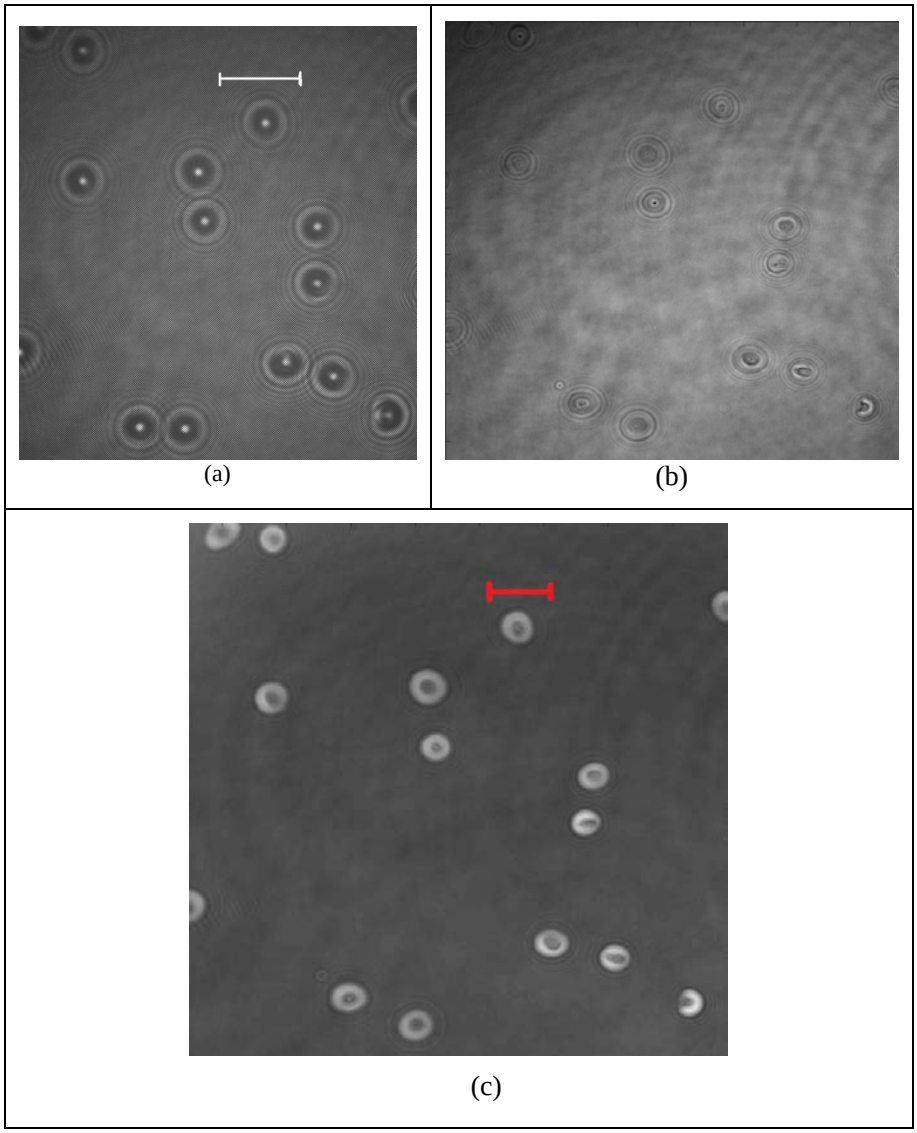

Figure 3.1: (a) Holographic image of RBC sanple(white line is 50μm in CCD plan), (b) intensity image, (c) phase image(red line is 10 μm in image plan);

To study cells we can study them in three measurement units. The first one is the phase value which can be used directly from Eq.2. The second way to measure the cell changes is to use OPD values which can be expressed by:

$$OPD(x,y) = d(x,y) \times \left[n_c(x,y) - n_m \right], \tag{3}$$

In which *d(x,y)* denotes the cell thickness, $n_c(x,y)$ is the mean intracellular refractive index integrated along the optical axis at the *(x,y)* position and n_m is the refractive index of the surrounding culture medium. Simply put, Eq. (3) means that the OPD signal is proportional to both the cell thickness and the intracellular refractive index, a property linked to the protein and water content of the cells [20, 49]. The last measurement unit is the real thickness of cell. Converting OPD or phase values to thickness values requires knowing refractive index of the specimen and the surrounding medium. It has been shown that for certain cells, such as red blood cells, in which a constant refractive index can be assumed for the entire cell contents, the thickness profile can be directly obtained from the phase profile or OPD profile. The reason is that RBC has no nucleus and must of it is the protein called hemoglobin [50]. The conversion can be done by following:

$$h(i,j) = \frac{\varphi(i,j) \times \lambda}{2\pi(n_{rbc} - n_m)}, \tag{4}$$

Where λ is wavelength of light source, $\varphi(i,j)$ is phase value in radians, and the refractive index of RBCs, n_{rbc}, has been measured with a dual-wavelength digital holographic microscopy. Here, n_{rbc} is 1.396 with no significant difference between groups of different ages. The index of refraction of the HEPA medium, n_m, is 1.3334[23].

A. Quantitative investigation of red blood cell three-dimensional geometric and chemical changes in the storage lesion using digital holographic microscopy

a. Abstract:

Quantitative phase information obtained by digital holographic microscopy (DHM) can provide new insight into the functions and morphology of single red blood cells (RBCs). Since the functionality of a RBC is related to its three-dimensional (3-D) shape, quantitative 3-D geometric changes induced by storage time can help hematologists realize its optimal functionality period. We quantitatively investigate RBC 3-D geometric changes in the storage lesion using DHM. Pathological changes in blood during storage, often called the blood storage lesion, is a rapidly growing area of biomedical research. Stored red blood cells undergo morphologic changes, metabolic alterations, and some degree of hemolysis during storage. During storage, red blood cells undergo depletion of potassium, 2,3-diphosphoglycerate, ATP, lipids and membrane, with increased red cell rigidity and impaired oxygen delivery. The stored units accumulate microvesicles derived from red cells, free hemoglobin and biologically active lipids, demonstrating increased pro-inflammatory and procoagulant activity. Modern blood bank preservative solutions provide glucose and other stabilizing substances to minimize these undesirable changes that might adversely affect the transfusion recipient [51]. Our experimental results show that the substantial geometric transformation of the biconcave-shaped RBCs to the spherocyte occurs due to RBC storage lesion. This transformation leads to progressive loss of cell surface area, surface-to-volume ratio, and functionality of RBCs. Furthermore, our quantitative analysis shows that there are significant correlations between chemical and morphological properties of RBCs.

b. Motivations:

In the human body, red blood cells (RBCs) serve many purposes, but one of the most important functions of RBCs is to transport oxygen and carbon dioxide between the lungs and the rest of the body's tissues. Every aspect of a RBC, including metabolism, size, and shape, is adapted to maximize functionality. Importantly, the RBC's shape should be optimal for maximal deformation, maximum surface at a given volume, rapid changes, and survival of the cell during its many repeated passages through the narrow channels. In fact, surface area is one of the most important properties of RBCs, since the exchange of oxygen and carbon dioxide takes place at their surface; larger surface area allows for an increased exchange of oxygen and carbon dioxide in the lungs and within the body cells. These conditions are satisfied by a biconcave disk shape, which is considered the medical norm for RBCs. The biconcave RBC has a flexible membrane with a high surface-to-volume ratio (SVR) that facilitates large, reversible, elastic deformation of the RBC as it repeatedly passes through small capillaries during microcirculation. In particular, the biconcave shape of RBCs is regarded as the result of minimizing the free energy of membranes under area and volume constraints, since there are no complex inner structures within RBC. However, during the storage period, RBCs and their preservative media suffer metabolic, biochemical, biomechanical, and molecular changes, commonly referred to as storage lesions. Furthermore, a large range of adverse effects related to RBC storage have been reported in critically ill patients when the RBC storage period exceeds 4 weeks. These effects include increased mortality, nosocomial infections, multiple organ failure, renal failure, and deep vein thrombosis. Much scientific evidence, however, supports that during the storage period, the RBC structure undergoes essential changes in shape: from biconcave disc to flat disk, and finally to a spherocyte, which leads to the inability of the RBCs to carry oxygen. Although a number of studies in recent years have analyzed changes in RBCs throughout their lifespan, most have not specified accurate quantitative

morphological and surface-to-volume rate-related changes, which are considered vital in terms of the performance of RBCs [23, 31-33].

In this section, the morphological and chemical parameters of individual RBCs are simultaneously obtained by using noninvasive and label-free DHM technique. The morphological and chemical parameters of RBCs in single-cell level with different ages are automatically quantified. We investigate 3-D geometric features of RBCs including surface area, sphericity index, morphological functionality factor, sphericity coefficient, and SVR in storage lesion. In addition, the correlation analysis between chemical parameters of MCH/MCH concentration and morphological parameters of RBCs in different ages is presented. The datasets utilized for our study consist of healthy blood samples stored for 8, 13, 16, 23, 27, 30, 34, 37, 40, 47, and 57 days and are divided into 11 classes of RBCs stored in 11 different periods. The 11 classes, overall, have more than 3300 RBCs, with more than 300 RBCs per each class. To calculate 3-D geometric parameters of RBCs, a marker-controlled watershed segmentation algorithm is utilized, which removed the unnecessary background, segmenting reconstructed images into many single RBCs(See Fig.3.2). Finally, morphological and chemical parameters of each single RBC for the various storage times are calculated, and the results are compared against each other. Our findings show that in storage lesion, the structure of an RBC goes through essential changes in terms of shape, i.e., from a biconcave disc to a spherocyte. Interestingly, our experimental results indicate that the surface area values of normal RBCs obtained through DHM approximately agree with the values reported by other methods. These experimental results can contribute to the understanding of the changes in 3-D geometric features of RBCs during the storage period and can provide quantitative information to support the work of hematologists [23].

c. RBC preparations and mathematics

RBC preparations

The blood sample was donated by a healthy person and was stored in a transfusion bag. These RBCs were obtained from the Service Régional Vaudois de Transfusion Sanguine in Switzerland. The RBCs were stored at 4°C during the storage period. The RBC concentrate was extracted from the blood transfusion bag and diluted in HEPA buffer (15-mM HEPES pH 7.4, 130-mM NaCl, 5.4-mM KCl, 10-mM glucose, 1-mM CaCl2, 0.5-mM MgCl2, and 1-mg⁄mL bovine serum albumin) at a concentration of approximately 0.15%. Then, 0.2 mL of the RBC suspension were introduced into the experimental chamber, which itself consisted of two coverslips separated by spacers 1.2-mm thick. In order to allow for the sedimentation of the cells on the bottom coverslip, cells were incubated for 30 min at a temperature of 37°C before mounting the chamber on the DHM stage. All experiments were conducted at room temperature [23].

Equations:

To characterize the 3D geometric quantities of erythrocytes at different storage periods, a sphericity coefficient k, a ratio of the erythrocyte thickness at the center d_c to the thickness at half of its radius d_r (dimple area), is determined as follows:

$$k = \frac{d_c}{d_r}. \tag{5}$$

The sphericity coefficient k can determine three types of erythrocytes. A value of k less than unity leads to biconcave erythrocytes, a value around unity denotes a flat disk erythrocyte, and a value greater than unity specifies a spherocyte. A k factor of around 0.35 has been reported for healthy erythrocytes and around 1.12 for the sick ones.

Surface area is the area of a surface or collection of surfaces bounding a solid. There are different formulas for calculating the surface area of regular shapes. Generally, the surface area with the form of a function $z=f(x,y)$ can be calculated as follows:

$$Surface\ Area = \iint_S \sqrt{\left(\frac{\partial z}{\partial x}\right)^2 + \left(\frac{\partial z}{\partial y}\right)^2 + 1}\ \ dA, \tag{6}$$

where the integral is taken over the entire surface. For irregular shapes, like the ones of RBCs, however, many methods have been proposed. These methods typically split and divide irregular surfaces into smaller regular areas and add these smaller areas to give the entire surface area. Understandably, the accuracy of such a calculation is dependent on the smaller area chosen. In most cases, covering the entire surface area of an RBC by small triangles can provide a high accuracy (Error is less than 5%). The surface area of any of these triangles can be calculated easily by some popular methods, such as the Heron formula, which uses the length of each side of a triangle, using the base and height side, using one side of an equilateral triangle, or using the lengths of two sides and the included angle. If we have a triangle whose sides have lengths a, b, and c, the Heron formula states that:

$$Surface\ Area = \sqrt{s(s-a)(s-b)(s-c)}, \tag{7}$$

where s is $\frac{a+b+c}{2}$. In this research, the surface area of each triangle is calculated by Eq. (3). Our experimental results show that Eq. (3) is accurate enough for the RBC surface area calculation. The total surface area of an RBC in DHM consists of the surface area of the top view summed with the projected surface area of the top view. The projected surface area (*PSA*) is defined to be as follows:

$$PSA = Np^2, \tag{8}$$

where p denotes the pixel size in the DHM phase image (here p = 0.159 μm) and N is the total number of pixels within an erythrocyte. *PSA* is reported to be around 45±5 μm^2 for normal RBCs [31], and can also be used to estimate the radius of an RBC. The RBC radius (r) has been estimated here by considering the radius of a circle having the area of the PSA of a RBC:

$$r \cong \sqrt{\frac{PSA}{\pi}}, \tag{9}$$

The surface area for the top view of an RBC (see Fig. 3.2) can be computed by different methods; for the purpose of our study, the top view is partitioned into small triangles as mentioned earlier, and a summation of the areas of all the small triangles determines the surface area of the top view.

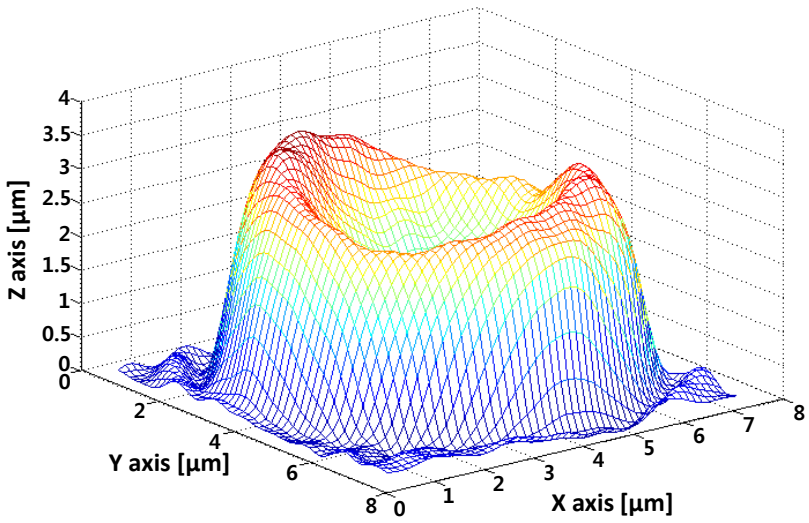

Figure 3.2: 3-D view of an RBC obtained by the DHM method

Accordingly, the total surface area of a single RBC can be computed as follow:

$$SA = PSA + TVSA\,, \tag{10}$$

where *PSA* is the projected surface area and *TVSA* is the surface area of the top view. Our measurement of the surface area is within the range of the previously reported value. Fig.4 shows some sample at different storage time and their respective surface area's histogram. It shows the variation in size and shape of red cells stored. By days 40 and 57 of storage (Fig.3.3 (i)-(k)) the RBCs range from large and misshapen to small spherocyte cells. Indeed, leftward shift of the normal distribution implies that RBC's surface area is dropping while storage time is increasing.

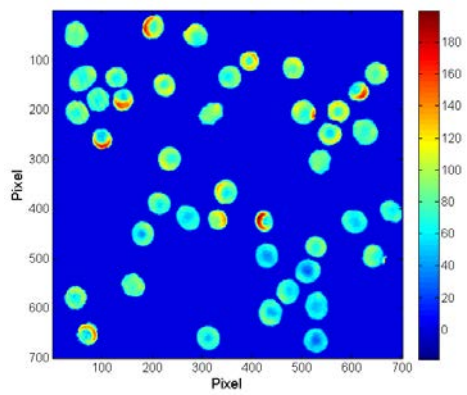

(a)

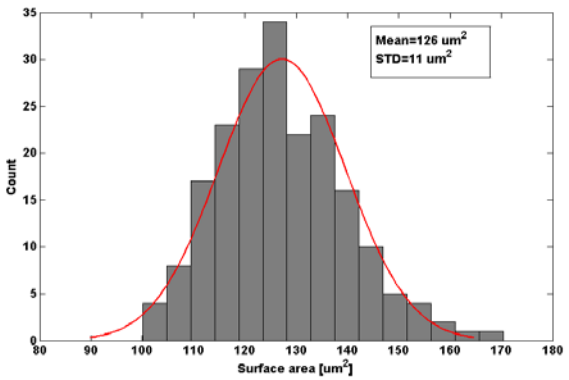

(b)

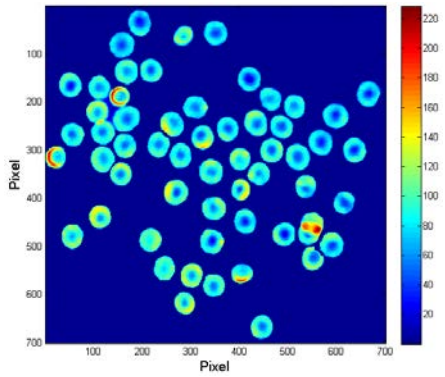

(c)

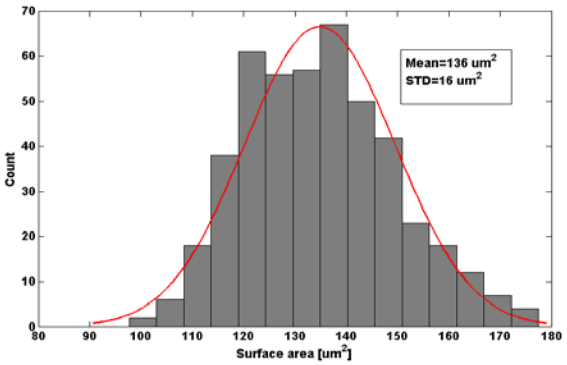

(d)

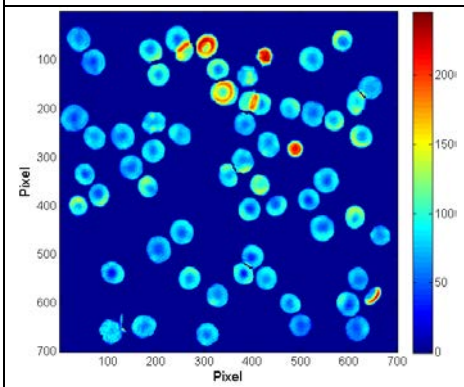

(e)

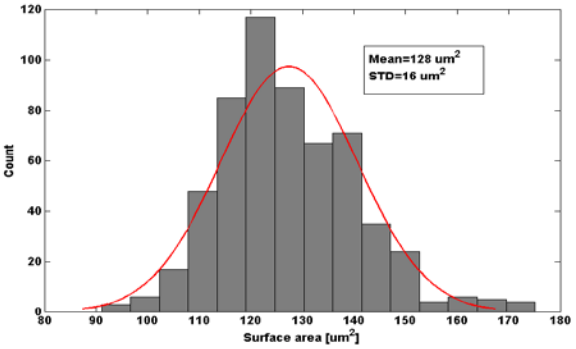

(f)

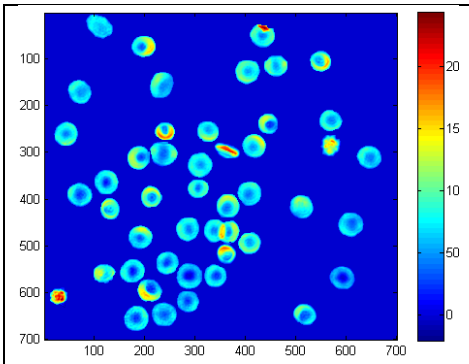

(g)

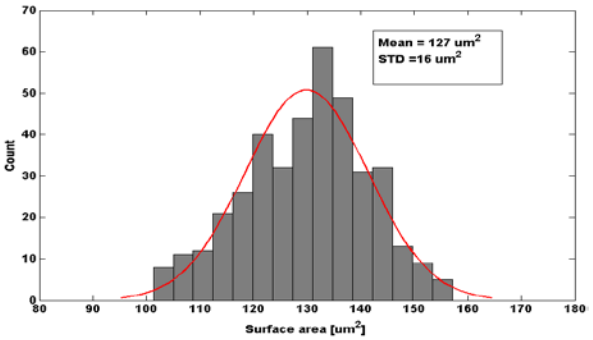

(h)

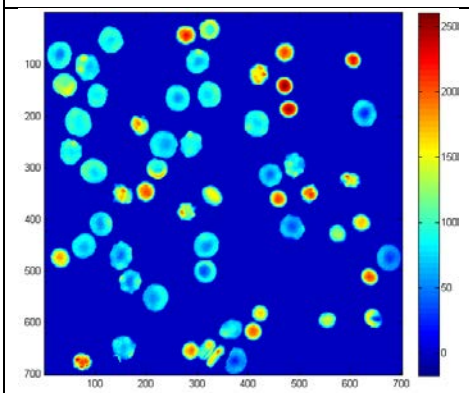

(i)

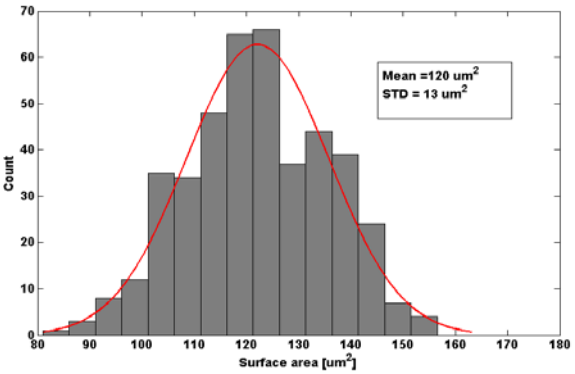

(j)

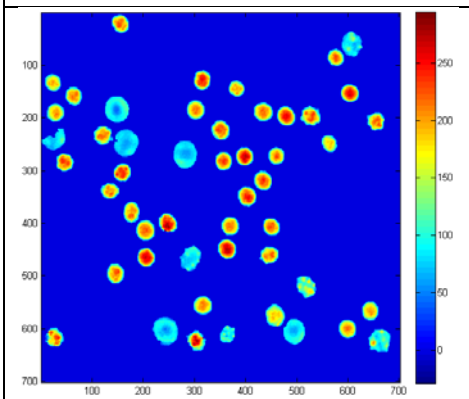

(k)

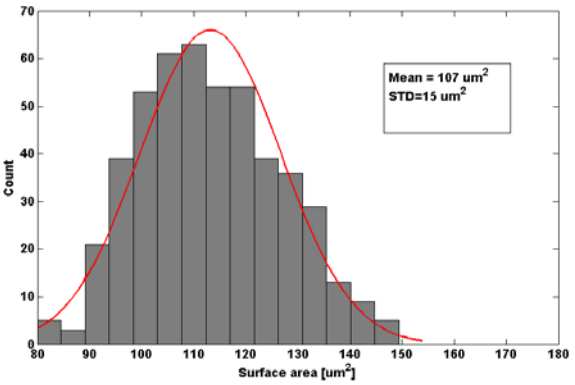

(l)

Figure 3.3:Different storage time and histogram of the surface area; (a), (c), (e), (g), (i) and (k) are RBC's with 8, 16, 23, 30, 40 and 57 days of storage, respectively. (b), (d), (f), (h), (j) and (k) are surface areas' histograms at the same storage time.

With the calculated surface area for an erythrocyte, we can estimate the morphological functionality factor f of the erythrocyte, which is the ratio of the RBC surface area to the surface area of a spherocyte with the same volume:

$$f = \frac{SA}{S_s} = \frac{SA}{4\pi r^2}, \tag{11}$$

Where SA can be calculated by Eq. (10) and S_s is the surface area of the sphere with radius r. An f value around unity characterizes a spherocyte. Moreover, taking into consideration Eq. (10), we can calculate the total surface area of all the blood erythrocytes S_t, which determines oxygen capacity of blood. The S_t is equal to the product of the number of erythrocytes in blood M and the arithmetic mean surface area SA_m of RBCs:

$$S_t = M \times SA_m . \tag{12}$$

Eq. (10) can be applied to obtain the SVR, which is a critical parameter for an erythrocyte because the higher the SVR, the more material a cell can exchange with its surroundings. The volume of RBC in a DHM phase image is denoted as:

$$V \cong \frac{p^2 \lambda \sum_{i=1}^{k} \sum_{j=1}^{l} \varphi(i, j)}{2\pi (n_{rbc} - n_m)}, \tag{13}$$

where p denotes the pixel size in the DHM phase image, k and l are the width and height of the phase image, λ is wavelength of the light source, $\varphi(i,j)$ is the phase value in radians, and refractive indices n_{rbc} and n_m are 1.396 and 1.3334, respectively. Another important parameter related to the shape of the RBCs is the sphericity index (dimensionless). Basically, it is the

measure of how spherical an object is, thereby giving an indication of how relatively rigid the RBC is. In addition, the sphericity index of each cell determines the degree of tolerance of that cell to deformation, for example, in passing through a narrow cylindrical channel. This parameter, also, can be useful in discriminating between healthy and pathological cells; for example, in identifying pathological cells in some hereditary diseases like spherocytosis. Deformability of cells can also be identified by measuring RBC mechanical parameters of fluctuations rate and shear stress. It has been shown that deformability of cells gradually decreases as cells are aging utilizing DHM technology. Thus, a determination of RBC deformability is the sphericity index, defined as follows:

$$SP = \frac{4\pi V^{2/3}}{(4\pi/3)^{2/3} SA}. \tag{14}$$

The mean value of the sphericity index of normal cells has been reported to be 0.79±0.026 at room temperature using interference microscopy. A similar value (0.73±0.02) has also been obtained using a micro-pipetting method. According to Eq. (14), the sphericity index is a dimensionless measurement from 0 to 1 where 0 is infinitely planar and 1 is perfectly spherical.

d. Results and discussions:

Morphological parameters measurements:

After segmenting and extracting the RBCs from the quantitative phase images, the surface area, volume, SVR, morphological functionality factor *f*, cell diameter, sphericity coefficient *k*, sphericity index *SP*, and oxygen capacity for all samples in the storage time as well as standard deviations were calculated. To reduce noise and increase the accuracy in Eq. (5), d_c and four adjacent values were averaged; d_r is the average of the some values (each one was chosen from

a different portion of dimple). Table.3.1 shows the calculated mean and standard deviation for all the 3-D geometric properties of RBCs with different ages. Figure 3.4 and Fig.3.5 show the morphological changes versus time.

Table 3.1: 3D geometric quantities of RBC in different storage days estimated by our proposed method

Property		Storage time[Days]										
		8	13	16	23	27	30	34	37	40	47	57
Surface Area (μm^2)	Mean	126	127	136	128	131	127	127	122	120	113	107
	STD	11	14	16	16	17	16	11	12	13	14	15
Volume (μm^3)	Mean	91	92	102	94	98	88	86	93	98	98	94
	STD	9	12	14	14	15	20	12	11	12	13	11
SVR (μm^{-1})	Mean	1.38	1.38	1.33	1.36	1.34	1.44	1.48	1.31	1.22	1.15	1.13
	STD	0.19	0.22	0.19	0.20	0.21	0.26	0.21	0.22	0.20	0.20	0.16
Cell Diameter (μm)	Mean	7.76	7.77	7.76	7.63	7.70	7.45	7.65	7.52	7.25	6.73	6.04
	STD	0.49	0.55	0.53	0.58	0.58	0.69	0.75	0.75	0.86	0.89	0.68
***k* factor**	Mean	0.88	0.78	0.66	0.84	0.70	0.69	0.93	0.93	1.03	1.20	1.35
	STD	0.18	0.19	0.21	0.22	0.23	0.25	0.30	0.24	0.34	0.36	0.41
***f* factor**	Mean	0.66	0.69	0.72	0.70	0.70	0.73	0.69	0.69	0.73	0.79	0.93
	STD	0.07	0.09	0.10	0.10	0.10	0.13	0.17	0.14	0.15	0.16	0.16
Sphericity Index	Mean	0.78	0.78	0.78	0.78	0.79	0.75	0.74	0.81	0.86	0.91	0.94
	STD	0.07	0.08	0.07	0.08	0.07	0.08	0.08	0.09	0.09	0.10	0.09

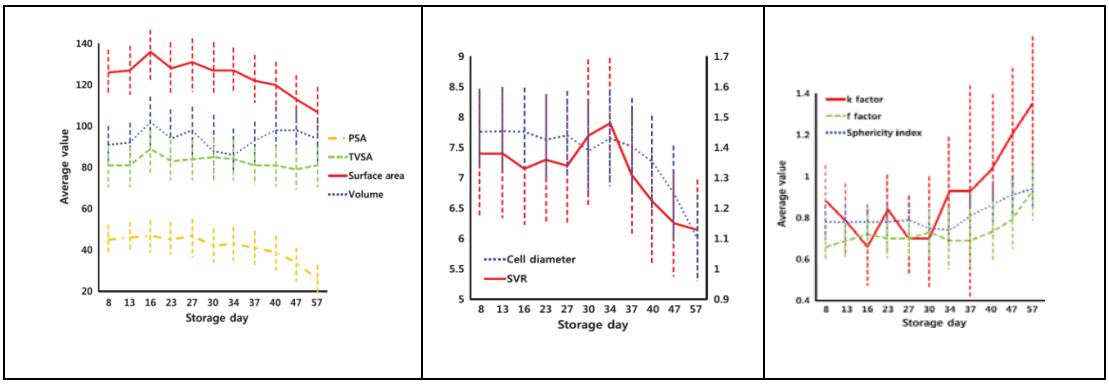

Figure 3.4: Changes of different morphological parameters

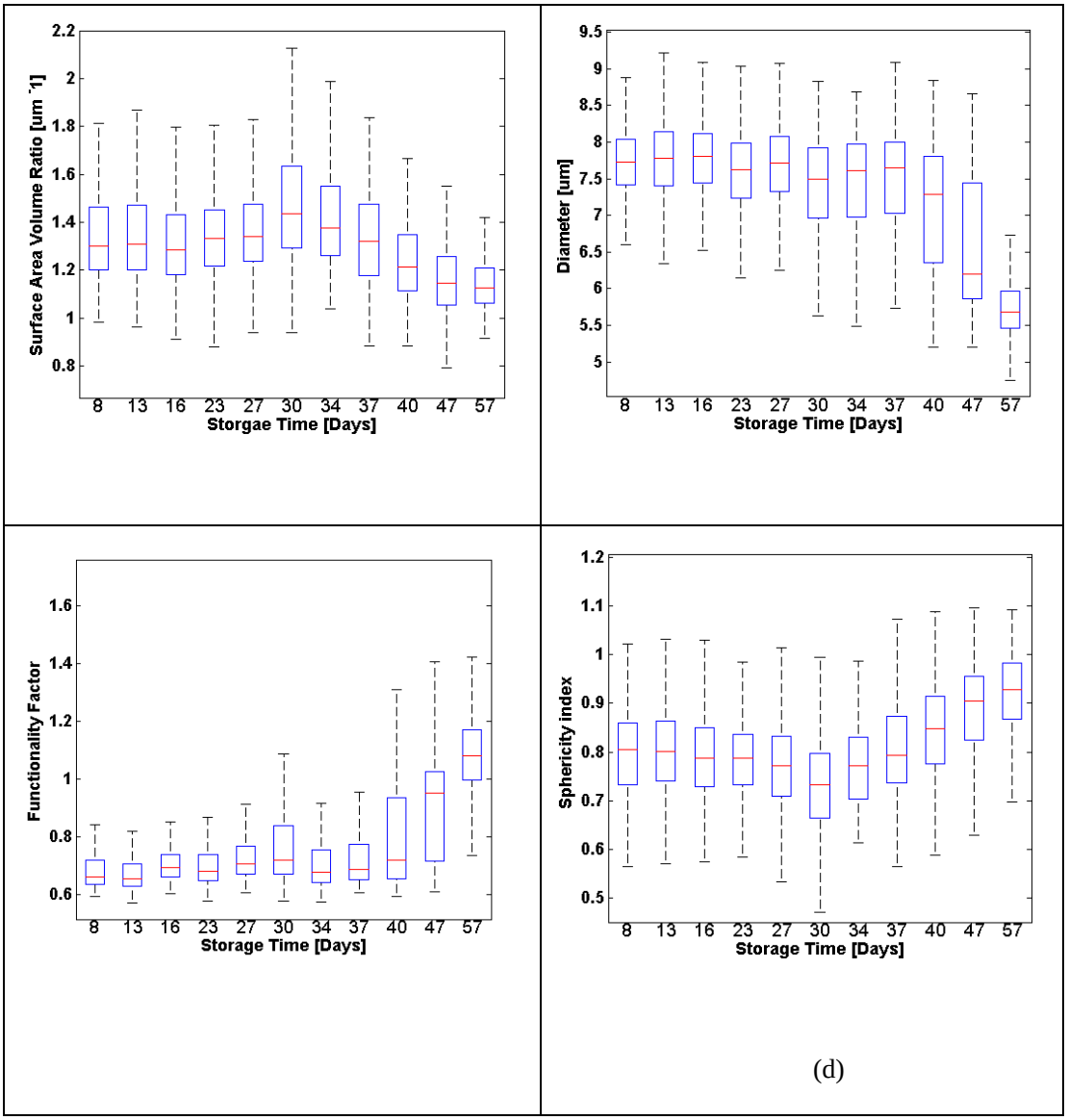

Figure 3.5: Box plot representation of the Morphological changes regarding storage time: (a) Surface area to volume ratio, (b) diameter changes, (c) functionality factor changes and (d) sphericity index changes. The box represents the median and the 25th and 75th percentile of the values; the whiskers represent the 10th and 90th percentile.

During the storage time, volume is only changing with a slight fluctuation that is

consistent with the previous clinical findings [53]. In contrasts while the diameter (Fig3.5(b)) decreases under almost fixed volume, the thickness value is increasing, which is consistent with previous findings [22]. Our measurement of the cell diameter is consistent with the previous findings (7.7±0.5 μm) [24]; however, while the cell diameter for the first five weeks is within this reported range, it begins to decrease when the storage time exceeds five weeks (Fig3.5(b)). Noted that in Fig3.5(b) and Fig3.5(c) the median value in 40 and 47 days is not around the center of the box representation. It mentions that there are two groups of cell in the respective storage time since it is the transition time for RBCs (42 days). Even though there is a small cell-cell variation within each class, the *t*-test showed no significant difference ($p<0.01$ for all samples). The SVR (Fig3.5(a)), which is an important characteristic for RBCs, is decreasing, since its volume remains relatively constant while its surface area is dropping. Most biological cells maximize the SRV to preserve their biological processes. It is noted that the SVR in the RBC within the first four weeks of storage is approximately 1.59±0.12. Aside from the presence of hemoglobin, the cell surface area or SVR is one important factor in the oxygen-carrying processes of erythrocytes. The effect of a smaller available surface area is clearly seen in terms of the oxygen capacity, which can be estimated using the averaged surface area values for different storage periods according to Eq. (12). We found that the oxygen capacity for RBCs within a thirty-day storage period is approximately 15% larger than that for RBCs with a storage period over six weeks, assuming an equal number of RBCs for each storage day (data not shown).

The *k* factor (sphericity coefficient) starts from a value less than one and increases gradually to a value greater than one. This means erythrocytes are biconcave initially and as storage time exceeds five weeks, they become flat disks and finally transform into spherocytes.

In contrast, the functionality factor *f* has the same trend as the sphericity coefficient in the way that *f* approaches unity. This means that the surface area of erythrocytes is almost equal to a sphere having the same radius. The sphericity index, which determines deformability, has the same trend as the functionality factor and the sphericity coefficient, since it rises after the first five weeks of storage. As it has been mentioned, if red cells are spherical, any deformation at all increases the surface area, and therefore nonsphericity is essential to the tolerance of erythrocytes to deformation in the circulation [31-33, 53]. Our finding about sphericity index says that during storage time sphericity index rises which implies less tolerance during passing through narrow channels. Modifications in the morphological functionality factor *f*, along with the sphericity coefficient *k*, consistently say that erythrocytes transform from biconcave into spherocyte. The morphological functionality factor *f*, sphericity coefficient *k*, and sphericity index are very important since they can specify the shape, type, and deformability of RBCs under aging, respectively. Variations in *k* in the first five weeks of the storage period may have been due to either inaccuracies in finding the accurate values of r_c and r_d,, although some pixels were averaged (each single cell contains maximum 70x70 pixels), or existence of stomatocyte RBCs. In many studies, it has been established that the normal RBCs (biconcave) undergo transformations in shapes toward stomatocytes upon variations in some of their chemical components; for example, increases in the medium's pH and additions of amphiphiles or even changes in temperature [58]. Findings about *k* and *f* and sphericity index are consistent in this research, and mentions that erythrocytes are transforming into spherocytes that causes a decrease in the functionality with respect to materials exchange between the tissues and lungs.

2D correlation analyses between the morphological and chemical parameters:

The promising ability of DHM technique is not limited only to measuring morphological parameters. Previously, it is shown that mean corpuscular hemoglobin (MCH) of RBCs can be measured by calculating dry mass of the RBCs since RBCs are mainly composed of hemoglobin [23].

$$MCH = \frac{10\varphi\lambda PSA}{2\pi\alpha_{Hb}} \tag{15}$$

Where φ is the mean phase shift induced by the whole cell, λis the wavelength of the light source of the setup, *PSA* is the projected cell surface, and α_{Hb} =0.00196 dl/g is a constant known as the specific refraction increment (in m3/kg or dl/g) related mainly to the protein concentration [23].

The mean corpuscular hemoglobin concentration (MCHC), a measure of the concentration of hemoglobin in a given volume can be measured by the following:

$$MCHC = \frac{MCH}{MCV} \tag{16}$$

It turns out that MCH and MCHC do not have significant changes during the storage time changes. They just fluctuate around their mean value (data not show). Our results indicate that, while cells can undergo small morphological changes during storage, they do not lose hemoglobin into the storage solution.

Since the chemical and morphological parameters are measured simultaneously at the single-cell level, we can evaluate correlation analysis between these parameters. We divided our samples into two different groups according to their storage time for the sake of clear visualization. Former contains two classes of 8 and 30 days and latter includes 47 and 57 days DHM data. Fig.3.6 presents the correlation analyses between the morphological and chemical

parameters of the groups. The correlations between the RBC parameters enable understanding of the cellular physiology of RBCs in detail.

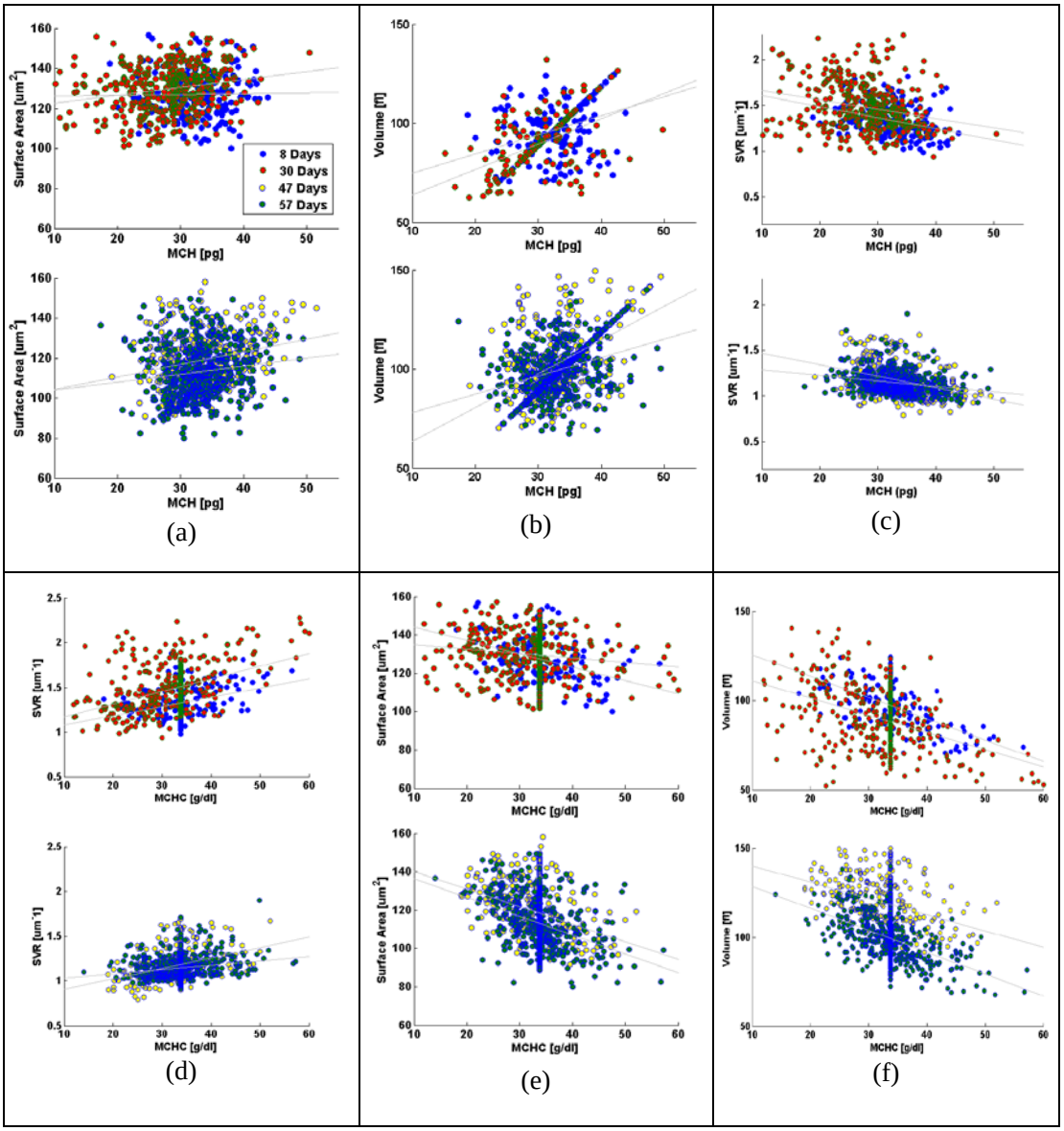

Figure 3.6: Correlation between Chemical-Morphological and Morphological-Morphological properties (The gray lines show linear relationship): (a) surface area and MCH, (b) volume and MCH, (c) SVR and MCH, (d) SVR and MCH, (e) surface area and MCHC, (f) volume and MCHC

MCH and MCHC correlation with morphological parameters:

Our correlation analyses exhibit that there is a positive correlation between MCH and surface area ($p<0.01$) (Fig.3.6 (a)), and a significantly strong positive correlation ($p<0.01$) between MCH and volume (Fig.3.6 (b)) consistent to the previous finding [59, 60]. It is worth to say that correlation coefficient has small fluctuations and the slope of regression line changes in the stored lesion. It is interesting to observe that RBCs with higher MCHC exhibited lower values in their surface areas and volumes (Fig.3.6(e)&(f)) in all ages, which is consistent with the previous research undertaken for populated cells [35]. Noted that correlation coefficient of surface area and MCHC value is smaller than the respective volume and MCHC at the same time. Moreover, our analysis shows that there is no significant correlation between functionality factor-MCH and functionality factor-MCHC while RBCs are aging ($p>0.01$). Furthermore, it turns out that sphericity index follows the same trend of functionality factor similar to the previous finding [35]. Interestingly, RBCs with higher MCH exhibited lower values in their SVRs in all ages (Fig.3.6 (c)). However, higher MCHC RBCs exhibit higher values in their SVR (Fig.3.6 (e)).

Correlation between Morphological Parameters:

The correlations between the RBCs' morphological parameters also demonstrated that they could enable us into better understanding of storage lesion. It has been shown in the previous research that there is a significant positive correlation between volume-diameter and

surface area-diameter [57]. Correlation analysis in this research reveals the same trend (data not shown). However, unlike Canham et.al [57] we realized that relation is not linear and tends to follow a nonlinear relation similar to the cell geometry. It means that for both area and volume plotted against diameter, the data are better presented by a quadratic and cubic equation, respectively. We also realized that correlation between surface area and diameter is significant ($p<0.01$) compared to the correlation between volume and diameter. We also found out that surface area and volume have significant positive correlation that implies that cells with higher volume can have bigger surface area. Interestingly, when storage time is 57 days we can see that correlation coefficient between volume and surface area is higher than other days (Table3.2).

Table 3.2: Regression results: $p<0.01$ for all data

Property	Storage time[Days]										
	8	13	16	23	27	30	34	37	40	47	57
Surface area vs. Diameter	0.71	0.67	0.57	0.61	0.62	0.51	0.69	0.65	0.70	0.71	0.57
Volume vs. Diameter	0.25	0.33	0.35	0.28	0.43	0.14	0.27	0.14	0.16	0.27	0.23
Volume vs. Surface area	0.41	0.46	0.55	0.54	0.58	0.47	0.60	0.40	0.48	0.55	0.64

The sphere has a low SVR, whereas a high SVR is required to promote rapid diffusion of oxygen and carbon dioxide. The biconcave, however, allows the RBCs large surface area for exchanging metabolic products across the membrane and cytoskeleton, and results in their slight deformation. The RBCs need to be deformable so that they can stretch as they undergo distortions under mechanical stress during their circulation through narrow channels. However, spherocytes with less surface area suffer from less deformability. Besides this, the viscosity of the spherocytic cells is higher than that of the biconcave RBCs, which causes high resistance

during their passage through narrow channels. Significant chemical evidence can support this alteration during storage lesion. ATP levels fall away from the first week onwards and reactive oxygen species (ROS) levels rapidly increase to a maximum by the second week of storage lesion. Oxidation, correlated to vesicle release, is shown to reduce the spectrin interactions during storage lesion. Gathering of the mobile pool 3-band agrees with elevated ROS and oxidation of the RBCs and occurs before vesiculation. As much as RBCs lose membrane and become spherical throughout storage, deformability of stored RBCs decreases [60]. The findings in this research show that erythrocytes become spherocytes, lose surface area, and are around 20% and less deformable (elevated sphericity index) as their storage time exceeds five weeks.

e. Conclusion

We have estimated the 3D geometric quantities related to the shape, type, and functionality of RBCs in storage lesion using digital holography microscopy. Interestingly, the surface area values measured through our method are in approximate agreement with the surface area reported by the other techniques in the past. In addition, the 3D geometric changes of erythrocytes in storage lesion have been investigated using the surface area value of RBCs. The investigation into the sphericity coefficient and morphological functionality factor along with the sphericity index shows that RBCs transform from biconcave to spherical as the storage time exceeds five weeks. The transition from biconcave to spherocyte is accompanied by a significant loss of surface area in a dramatic increase in the sphericity index and subsequently less functionality with respect to the exchanging of materials between tissues and organs. Our correlation analysis between chemical and morphological properties exhibits that surface area has significant negative correlation with MCHC value. Interestingly, sphericity index has no correlation with either MCH or MCHC value similar to the functionality factor. Furthermore, correlation between surface area and diameter is stronger than volume and diameter. In

addition, understanding these morphological and mechanical transitions is fundamental to membrane biology, RBC circulation, and basic studies of cellular mechanics.

B. Human red blood cell recognition enhancement with three-dimensional morphological features obtained by digital holographic imaging

a. Motivations:

Human blood contains different type of cells; however, red blood cells (RBC) or erythrocyte are the most abundant cell type. RBC contains hemoglobin which binds to either oxygen or carbon dioxide. This allows oxygen to be transported to tissues and organs and carbon dioxide to be taken away during microcirculation. The biconcave shape of the erythrocyte is extremely important in the functionality of RBCs. It allows the membrane to have a high surface area to volume (SAV) ratio facilitating large reversible elastic deformation of the RBC while squeezing through the tiny capillaries. According to its importance, it has drawn considerable attentions into the pathology research in the clinical relevant blood diseases. Pathological disorders can modify RBCs and lead to significant alterations in its original shape. The consequences of modified RBC often are observed as clinical symptoms ranges from obstruction of capillaries and restriction of blood flow to tissues to necrosis and organ critical damages [31-39]. Also, counting cell types in the blood sample is another important task for investigating clinical status which can be evaluated by well-known methods such as complete blood count (CBC) or RBC distribution width (RDW) which are part of cytometry field. Because an automated cell counter samples and counts so many cells, the results are reliable in most of the cases [40]. However, certain abnormal cells in the blood may

not be identified correctly, requiring manual review and identification of any abnormal RBCs the instrument could not categorize. This information can be very helpful regarding identifying the cause of a patient's anemia. Abnormal increases or decreases in RBC counts as revealed in a complete RBC count may indicate that you have an underlying medical condition that calls for further evaluation.

In the case of RBC, biconcaves are substantial type in a healthy person, but there are other RBCs types with the different percentage varying between healthy and non-healthy persons. It has been shown that the percentages of different types of RBCs will be distinct according to the RBC diseases type [40]. Accordingly, it is essential to measure the percentage of each RBC type in a blood sample consists of multiple RBCs for diagnosis and drug testing subjects. Typically, the diagnosing is performed by a human expert, and it shows some drawbacks such as time-cost consuming and inaccuracy. Generally, experts visualize the sample, in the images through microscope based on their subjective knowledge from the viewpoint of intensity, morphology, texture etc. based features. Usually, small-scale differences in the features are overlooked by human eyes especially for the border-line diagnostic scenario.

However, the situation has changed completely by emerging of automatic classification algorithms. These techniques have been applied to problems in biology and have shown promising results for automatic recognition, classification of various micro-organisms [7-10]. Among the classification methods, the pattern recognition neural network (PRNN) has been suggested in non-linear classification problems such as RBC classification and counting [61-63]. The fundamental benefit of artificial neural network (ANN) is nothing but it does not use any mathematical model since ANN learns from data sets and identifies patterns in a sequence of input and output data without any previous assumptions about their type and interrelations. Also, ANN eliminates the drawbacks of the conventional methods by extracting the wanted information using the input data.

In conventional RBC classification problems, the experts deal with two-dimensional (2D)

erythrocyte images obtained by conventional microscopes and cameras [64-67]. These methods generally have good performance but most of them have a significant number of features since they need to discriminate groups by utilizing 2D features. However, in the case of RBC which is transparent or semi-transparent, we cannot take advantages of conventional intensity-based microscopes. Therefore, we believe that to obtain a satisfied level of accuracy, the classification and recognition should also take into account three-dimensional (3D) shape of RBCs. Among the techniques that can provide 3D images of transparent or semi-transparent cells digital holographic microscopy (DHM) has shown promising results. Also, the DHM technique has been utilized in the classification of RBC using 2D and 3D feature since DHM can provide quantitative phase image. In studying RBC, DHM enables the measurement of 3D features, such as mean corpuscular volume (MCV), surface area, surface area to volume (SAV) ratio, functionality factor, sphericity index and sphericity coefficients. Chemical parameters of MCH and MCHSD can also be obtained thanks to DHM. Accordingly, we believe that any automated RBC classification that can distinguish different RBC types accurately should take into accounts the benefits of DHM imaging technique. Figure3.7 shows a reconstructed phase image of a sample consists of biconcave, flat-disc, and stomatocyte shape RBCs. This image shows that in a single sample it is possible to see RBC with different morphologies.

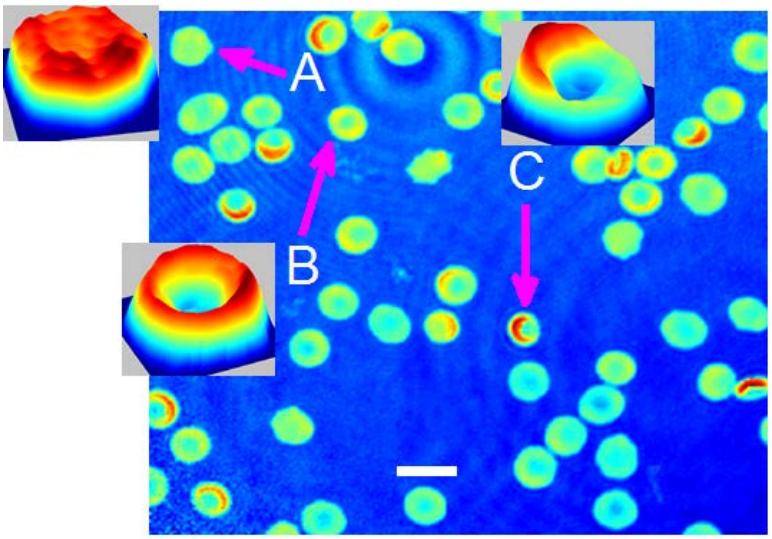

Figure 3.7: Reconstructed image and three different RBCs inside. A is a flat disc RBC, B is a biconcave RBC and C is a stomatocyte. White bar is 10μm.

In this study, four main types of RBC shapes, biconcave (doughnut shape), flat discs, stomatocyte and echino-spherocyte are interested RBCs for the quantitative determination of the percentage of RBC types in multiple human RBCs (See Fig.3.7). The reason for differentiating doughnut-shaped and flat-disc RBCs is that it can help in the applications of separating old cells versus young cells. It has been shown that during the stages of biconcave-echinocyte transformation in so-called storage lesion, biconcave cells become flat discs (loss of ATP results in a stiffer cytoskeleton that pulls the bilayer) after a few weeks of storage in blood bank. Transfusion of these old samples might have critical consequences according to the previous studies [38, 68].

At first, RBCs are visualized by off-axis DHM and the quantitative phase images are reconstructed by the numerical algorithm [30, 38]. Then, single RBCs are extracted from images with multiple RBCs using watershed algorithm [69]. At the next step, following 2D features of projected surface area (PSA), perimeter, radius, elongation, and PSA to perimeter rate are extracted. In this research, we have ignored extracting 2D features related to the inner

section of RBC, unlike the previous method proposed by [11-27], since flat-disc and echino-spherocyte RBCs do not have the inner section. Also, volume, surface area, SAV ratio, average RBC thickness, sphericity index, sphericity coefficient and functionality factors, and MCH and MCH surface density (chemical properties of RBC) are extracted from single RBCs. The latter feature-set is related to the morphological and biochemical properties of RBC 3D profile. Along with the 3D features, two new features related to the ring section of RBC are introduced. These features add significant information to the classification model and increase the discrimination power of the classifier. Then, each feature set is fed into PRNN, separately, and the classification results are compared using 10-fold cross validation (CV) technique. Since we are involved in a classification model with non-linear decision boundary, we have decided to use PRNN strategy. In PRNN, the training algorithm is Bayesian regulation back-propagation which updates the weights according to Levenberg-Marquardt optimization technique and the activation function for mid-level layers is hyperbolic tangent sigmoid.

Finally, to propose the best feature set, concerning both 2D and 3D features, sequential forward feature selection (SFFS) is utilized here. It has been shown that the best performance of a classification model can be achieved by selecting the most informative features and remove noisy ones that are either redundant or irrelevant [70]. Indeed, reducing the number of features can shorter training time, reduce the complexity of classifier and simplifies the model for interpretation goals. SFFS technique tries to select a subset of variables that best predict the data by sequentially selecting features until there is no improvement in the prediction.

In this research, we have extracted 108 biconcave RBCs from a healthy sample stored for 1 day in the blood bank, 106 samples of stomatocyte shape from a sample with predominantly of stomato cells, 38 samples of flat-disc shape and 71 samples of echino-spherocyte shape for training and testing PRNN. Flat-disc and echino-spherocyte cells are extracted from RBC samples stored in the blood bank for 40 days and 57 days, respectively. Performance comparison is evaluated by calculating miss-classification rate of 10-fold CV technique. It is

often claimed that leave-one-out-cross-validation (LOOCV) has higher variance than k-fold CV, and that it is because the training sets in LOOCV have more overlap. This makes the estimates from different folds more dependent than in the k-fold CV, hence increases the overall variance [71].

Our experimental results demonstrate that the PRNN trained by 3D features gives a good performance in classifying and counting RBCs in multiple human RBCs in an automated manner in comparisons with the 2D features. In addition, we introduce the best set of features which combines 2D and 3D features to improve the RBCs classification accuracy. We believe that the final feature set evaluated with the presented neural network classification strategy can provide better discrimination results.

b. Feature Extraction

Two-dimensional (2D) Features

After segmentation step and extracting many single RBCs, features can be extracted. We first start with 2D features. Following features are extracted in 2D case.

Table 3.3: 2D features descriptions.

	Feature Name	Description
2D-F1	Projected surface area (PSA)	PSA=$N\times p2$ (p is pixel size in holographic image and N is number of pixels within RBC)
2D-F2	Perimeter (Pr)	Length of the RBC boundary
2D-F3	Circularity (Ci)	$Ci = \frac{Pr^2}{PSA}$
2D-F4	Elongation (El)	Orientation of chain code in the cell boundary

2D-F5	Radios (R)	Radius is estimated by considering the radius of a circle having the area of the PSA $R = \sqrt{PSA/\pi}$
2D-F6	PSA/Perimeter (PSP)	$PSP = \frac{PSA}{Pr}$

Elongation of the RBC is a measure of the ratio of width to length for oblong RBCs. It can be computed from the chain code by summing the number of each type of element 0 to 7 and combining 0 and 4, 1 and 5, 2 and 6, and 3 and 7 [64].

Three-dimensional (3D) Features

Since some 3D features required thickness of the RBC, we first need to convert phase image into thickness image. Accordingly, the thickness value $h(i,j)$ for each pixel of (i,j) with phase value $\varphi(i,j)$ in a phase image can be expressed by Eq.4. Surface area is another important property and has the main contribution in different 3D features. Generally speaking, the surface area of the RBC is the surface area of the membrane mesh plus projected surface area. The method in this reseach splits and divides RBC surfaces into smaller regular areas (triangles here) and adds these smaller areas to give the entire surface area. Understandably, the accuracy of such a calculation is dependent on the smaller area chosen [23].

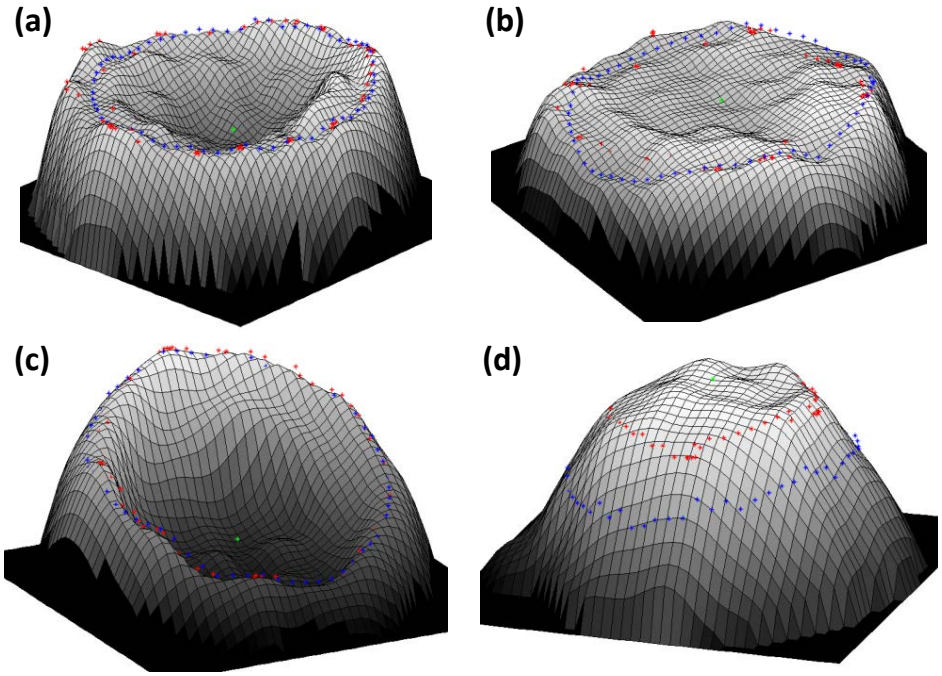

Figure 3.8: 3D representation of four RBC categories and points on the ring section, (a) shows a typical biconcave sample, (b) shows a flat disc in which center raised up, (c) shows a stomatocyte RBC and (d) is a spherocyte RBC.

3D features listed in Table 3.4 are extracted in this research. We only give a short description of the eight features related to the morphological properties of RBC, but interested readers can refer to [25, 27] for the detail of each feature. Regarding the calculation of three features (F9-F11), we obtained many points over the ring section of RBC by applying two techniques. First, we estimate the ring section (blue points in Fig. 3.8) by calculating the radius of a circle having the area of the projection of RBC on X-Y plane (the ring is around three fourth of the RBC radius). Then, we update the position of each point on estimated ring (blue points) by finding the thickest point in a 3×3 neighbor (red points in Fig. 3.8). From now on we name the red points as RPs. Single green point shows the center of RBC regarding the calculation of sphericity coefficient. In this study, we have decided to obtain 30 RP points. The reasons is that the total number of points on the ring section for the stomatocyte RBCs is between 90-120 points according to our calculation. Also, since we are looking at a 3x3

neighborhood around the blue point to find the point on the ring (red point) there is high possibility of overlapping between red points. For example, Fig.3.9 shows the position of red and blue points when we increase the number of points. We can see that by increasing the number of red points many of them overlap.

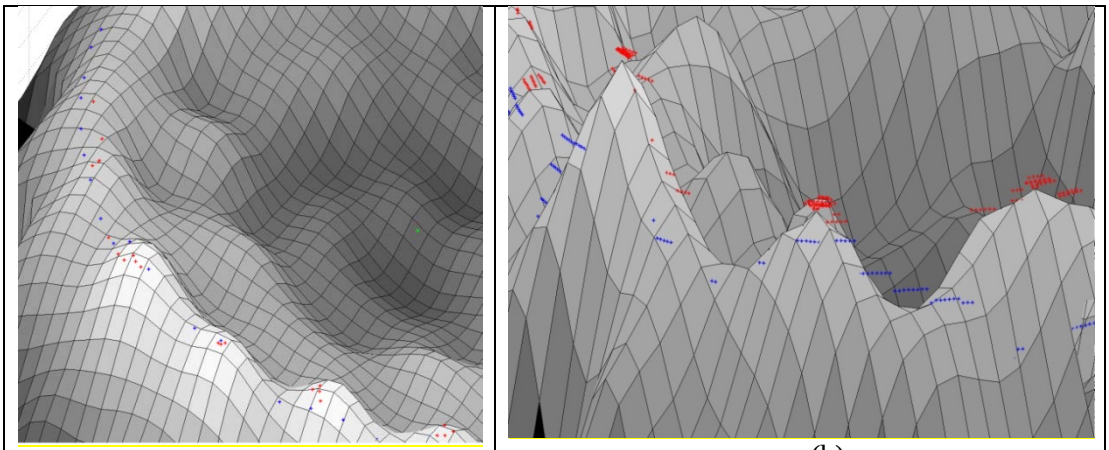

(a) (b)

Figure 3.9: 3D representation of RBC ring section with red and blue points on it. (a) number of points is 60, (b) number of points is 600.

Table 3.4: 3D features descriptions

	Feature name	**Description**
3D-F1	Average thickness (*AT*)	$AT = \frac{\sum_{i=1}^{k}\sum_{j=1}^{l} h(i,j)}{k \times l}$ ($h(i,j)$ is the thickness at $(i,j)^{th}$ pixel)
3D-F2	Volume (*V*)	$MCV \cong p^2 \sum_{i=1}^{k}\sum_{j=1}^{l} h(i,j)$
3D-F3	Top view surface area (*TVS*)	Surface area of the upper view of erythrocyte calculated by dividing surface into small triangles and then the summation of each triangle's surface area.

3D-F4	Top view surface area volume ratio	$TVSV = \frac{TVS}{V}$
3D-F5	Total surface area (*SA*)	$SA = TVS + PSA$
3D-F6	surface area volume ratio (*SAV*)	$SAV = \frac{SA}{V}$
3D-F7	Sphericity index (*SI*)	$SI = \frac{4\pi V^{2/3}}{(4\pi/3)^{2/3} SA}$
3D-F8	Functionality factor (*FF*)	$f = \frac{SA}{4\pi R^2}$
3D-F9	Sphericity coefficient (*SP*)	$SP = \frac{d_c}{d_r}$ (d_c and d_r are thickness values in RBC center and ring section, respectively)
3D-F10	*STD* of thickness in ring section	This feature measures variation in the thickness of *RP*s in the ring of RBC
3D-F11	Upper side of the ring/ lower side of ring	This feature is calculated by dividing four maximum *RP*s by four minimums
3D-F12	Mean hemoglobin (*MCH*)	$MCH = \frac{10\bar{\varphi}(PSA)}{2\pi\alpha}$ ($\bar{\varphi}$ is the average phase value, λ is the wavelength of the light source of the setup and α =0.00196 *dl*/*g* is a constant known as the specific refraction increment related to the protein concentration)

3D-F13	MCH surface density (*MCHSD*)	$MCHSD = \frac{MCH}{PSA}$

We believe that above 3D features can distinguish between different RBCs since they are related to the 3D profile of RBC. The statistic t-test using two-sample Kolmogorov-Smirnov test revealed that some of these features are independent (data not shown). Table3.5 shows average and STD values of each feature for each RBC type.

Table 3.5: 3D feature values (Mean±STD)

	Biconcave	Flat-disc	Stomatocyte	Echino-spherocyte
Average thickness (μm)	2.18±0.3	2.27±0.25	2.75±0.36	4.47±0.36
Volume (μm^3)	93.23±13	103.29±14.72	95.85±11.52	101.91±16.4
Top view surface area (μm^2)	103.85±15	94.50±9.62	106.04±12.39	95.65±10.6
Top view surface area volume ratio(μm^{-1})	1.12±0.09	0.92±0.05	1.11±0.1	0.95±0.06
Total SA (μm^2)	148.32±16.38	143.21±12.48	147.32±16.11	120.76±11.79
SA volume ratio (μm^{-1})	1.61±0.17	1.40±0.13	1.55±0.18	1.19±0.09
Sphericity Index (SI)	0.40±0.18	0.74±0.04	0.69±0.06	0.87±0.032
Functionality Factor (FF)	0.86±0.16	0.74±0.07	0.93±0.19	1.21±0.14
Sphericity Coefficient (SP)	0.67±0.05	0.82±0.06	0.5799±0.21	1.16±0.14
STD of thickness in ring section	0.0332±0.021	0.054±0.018	0.1321±0.096	0.1254±0.03
Upper side of the ring/	1.31±0.11	1.25±0.09	1.93±0.44	1.44±1.14

lower side of ring				
MCH (pg)	31.29±4.55	34.68±5.01	32.17±3.94	34.29±5.51
MCHSD(pg/μm^2)	0.68±0.1	0.71±0.08	0.85±11	1.39±0.11

c. Pattern Recognition Neural Network

Artificial neural networks (ANN) are highly simplified mathematical models of biological neural networks having the ability to learn and provide meaningful solutions to the problems with high-level complexity and nonlinearity. The ANN approach is faster compared to its conventional techniques, robust in noisy environments, and can solve a wide range of problems. Due to the advantages, ANNs have been used in numerous applications [61-63]. A typical ANN is presented in Fig. 3.10. An important application of neural networks is pattern recognition that can be implemented by using a feed-forward neural network with a specific training function and specific function in the output layer. During training, the network is trained to associate outputs with input patterns. When the network is used, it identifies the input pattern and tries to output the associated output pattern.

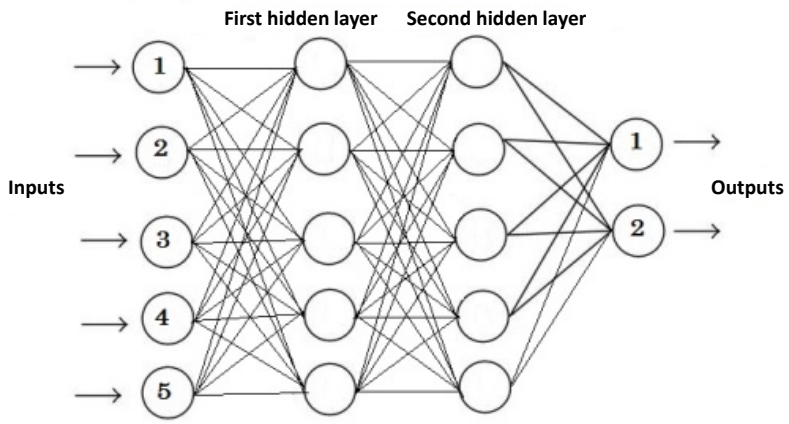

Figure 3.10: A feed-forward artificial neural network configuration with five input nodes, two output nodes, and two hidden layers.

The information processing in the ANN strategy starts from the input layer to the hidden layer (from one hidden layer to another one if there are more than one) and from the last hidden layer to the output layer. A synaptic weight is assigned to each link to represent the relative connection strength of two nodes at both ends in predicting the input-output relationship. y_j (the output) of any node j, is given as:

$$y_j = f\left(\sum_{i=1}^{n} W_i X_i + b_i\right), \tag{17}$$

where W_i is the connection weight, X_i denotes the i_{th} input of node j, n is the number inputs to node j and b_j is the bias value. Function f or so-called activation function determines the response of a node to the total input signal that is received. Generally, the activation function for hidden layer in pattern recognition neural network is hyperbolic tangent sigmoid transfer function due to the following advantages:

1- It limits the range of data to values between -1 and 1. This function is almost linear near the mean. It is smooth and has monotonic nonlinearity property at both extremes.

2- It remains differentiable everywhere and the sign of the derivative is unaffected by the normalization. Generally, the differentiable requirement is needed for hidden layers and hyperbolic tangent sigmoid transfer function is often recommended as being more balanced.

3- The 0 for hyperbolic tangent sigmoid transfer function is at the fastest point (highest gradient or gain) and not a trap.

4- The hyperbolic tangent sigmoid transfer function suit the output layer to the competitive outputs of softmax function.

5- Since it can be estimated by $\frac{2}{1+e^{-2x}} - 1$ it can be implemented faster in MATLAB.

For output layer in PRNN, the activation function is softmax transfer function (normalized exponential) that can be interpretable as posterior probabilities for a categorical target variable. It is highly desirable for those outputs to lie between zero and one and to sum to one. The purpose of the softmax activation function is to enforce these constraints on the outputs. Let the input to each output unit be q_l, $l=1,...,k$, where k is the number of classes. Then the softmax output y_l is:

$$y_l = \frac{e^{q_l}}{\sum_{m=1}^{k} e^{q_m}}. \tag{18}$$

According to Eq. (18) sum of all "y"s is equal to unity and can be interpreted as the posterior probability for the final decision. The training algorithm updates the weight and bias values according to Levenberg-Marquardt optimization. It minimizes a combination of squared errors and weights and then determines the correct combination so as to produce a network that generalizes well (Bayesian regularization) [72].

d. Experimental Results and Discussion

In this experiment, 108 RBCs are labeled as biconcaves, 106 RBCs labeled as stomatocytes, 38 RBCs are labeled as flat-disc and 71 RBCs labeled as echino-spherocytes. Four samples of each group are presented in Fig. 3.11. Simulations are all executed on a 64-bit Windows 7 computer with a 3.60 GHz Intel Core i7- 4790 CPU, 8 GB RAM, and 8 cores. The performance of the classification model is assessed by utilizing 10-fold CV check. Put it simply, the data set is divided into 10 subsets, and the test is repeated 10 times. Each time, one of the 10 subsets is used as the test set and the other 9 subsets are put together to form a training set. Then the average miss-classification error across all 10 trials can show the overall miss-classification error. PRNN consists of one input, output layer and three hidden layers. Number of neurons in each hidden layer respectively is five, ten and five. Neuron numbers are obtained by trial-and-error technique. All the simulations codes are implemented in MATLAB 2014.

Comparison between 2D and 3D features

In the case of 2D features (Table 3.3), 10-fold CV revealed that that the total misclassification rate is significantly high. In detail misclassification of each group is as following; flat-disc 64%, stomatocyte 13.4%, biconcave 32.3% and echino-spherocyte are 4.2%. Only echino-spherocyte RBCs can be accurately classified by taking into account 2D features while other categories have significant error. According to the confusion matrix, PRNN confuses between biconcaves and flat-discs by using 2D features (data not shown). In contrast 3D features explained in Table 3.4 generate more accurate and interesting results. According to the results of 10-fold cross validation, misclassification rates are 0%, 1.6%, 3.2% and 0% for flat-disc, stomatocyte, biconcave and echino-spherocyte RBCs, respectively.

Table.3.6 shows the classification error for 2D and 3D features. It is noted that the presented neural network classification strategy was used to evaluate the discrimination power of the feature set based on 3D morphological properties of RBC against 2D features. The classification results obtained with the neural network demonstrate that the 3D features can be more effective in RBC classification than the 2D features.

Table 3.6: Miss-classification results of 2D and 3D features

	Flat-disc	**Stomatocyte**	**Biconcave**	**Echino-spherocyte**
2D features	64%	13.4%	32.3%	4.2%
3D features	0%	1.6%	3.2%	0%

Table 3.7: Normalized mutual information between 2D features.

	2D-F1	**2D-F2**	**2D-F3**	**2D-F4**	**2D-F5**	**2D-F6**
2D- F1	1	0.61	0.13	0.37	0.31	0.33
2D- F2	0.61	1	0.057	0.25	0.071	0.37
2D- F3	0.13	0.057	1	0.12	0.7	0.014
2D- F4	0.37	0.25	0.12	1	0.15	0.14
2D- F5	0.31	0.071	0.7	0.15	1	0.04
2D- F6	0.33	0.37	0.014	0.14	0.04	1

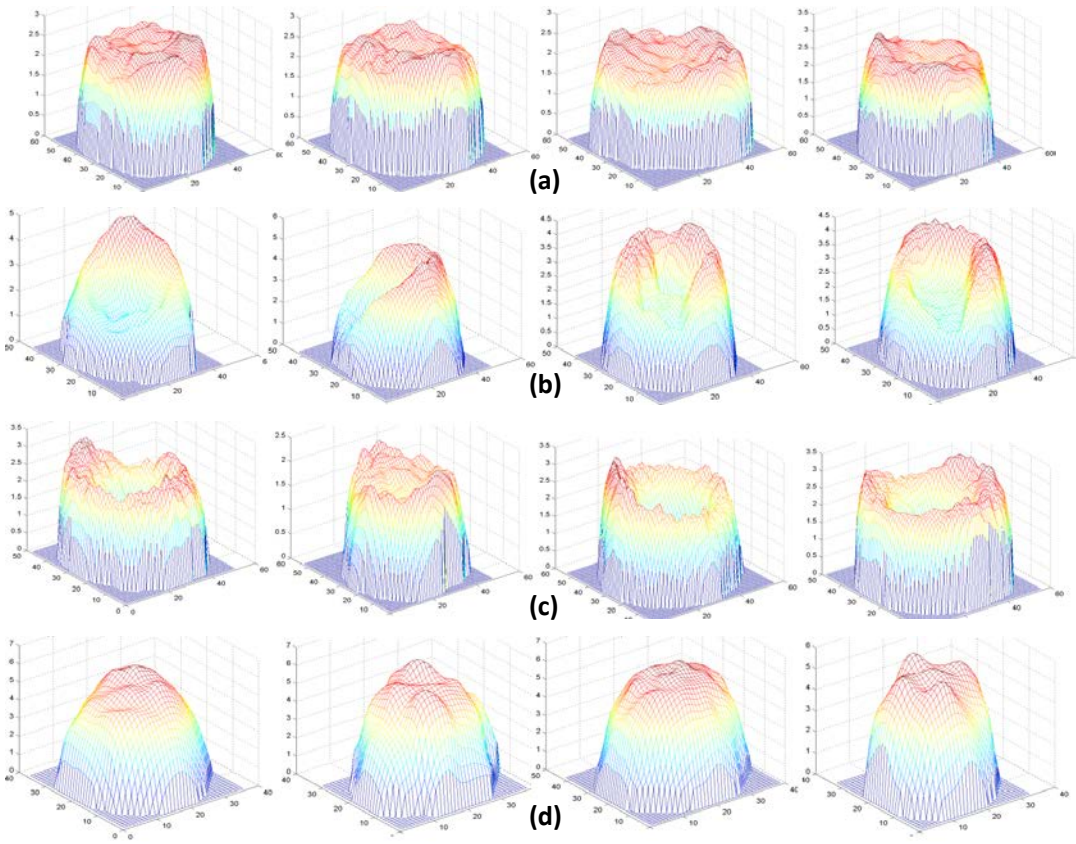

Figure 3.11: Samples of each RBC group used in this research; (a) four samples of flat disks, (b) four samples of stomatocyte morphology, (c) four samples of biconcave RBC and (d) four samples of sphero-echinocyte RBC.

In another experiment, we evaluated the normalized mutual information between each feature in 2D and 3D features. In the case of 2D features, it turns out, as shown in Table 5, that there is a big mutual information between some features. Mutual information is the amount of information that two features share. If the mutual information between the two features is large (small), the two features are closely (not closely) related. If the mutual information becomes zero, the two features are independent. For example, 2D-F1 has significant mutual information with features 2D-F2, 2D-F4, 2D-F5, 2D-F6 (see first row of the Table3.7). Therefore, this feature is statistically redundant and can not add significant information.

Combining 2D and 3D features and select the best feature-set

We believe that the best classification model should take into account not only 3D features but also 2D features. However, it is worth mentioning that not any feature can add significant information to the classification model. Therefore, we believe that the performance of any classification model can be enhanced by taking advantages of feature selection (FS) strategy. In FS we seek to find the best set of the features that has the strongest ability (or strong) to distinguish each class. Generally speaking, FS preserves the original features intact; features deemed unimportant/irrelevant/redundant are simply eliminated from further consideration while selecting only those features that significantly contribute to the classification problem. Therefore, FS can reduce the number of features (variables) of the classification problem and make the model simpler (or less complex) and shorten training time [70]. We also implemented FS in this research by using sequential forward feature selection technique (SFFS). Generally speaking, in SFFS features are sequentially added to an empty candidate set until the addition of further features does not decrease the criterion. It has two components of an objective function, called the criterion, and a sequential search algorithm. In former, common criteria are misclassification rate for classification objects (similar in this research) and mean squared error for regression models. A sequential forward search algorithm adds features from a candidate subset while evaluating the criterion. Since an exhaustive comparison of the criterion value at all 2^n subsets of an *n-feature* data set is typically infeasible (sometimes feasible but time-consuming), sequential searches grows the candidate set. It turns out that the following features of average RBC thickness (3D-F1), top view surface area volume ratio (3D-F4), sphericity coefficient (3D-F9), the upper side of the ring divided by lower side of the ring (3D-F11) and perimeter (2D-F2) can better classify multiple RBCs in this research. Our experimental results also revealed that adding more features does not add significant discrimination ability to the final classification model. As it has been mentioned earlier, SFFS is responsible for adding or removing features from the final feature set. One component of SFFS is the objective function

which here is the misclassification rate. SFFS starts from an empty set and add features one by one to the set and evaluates the misclassification rate. If there is a significant changes in the objective function (misclassification rate) then feature can be added to the final feature set (Table.3.8).

Table 3.8: Misclassification rate after adding each feature to the feature set.

Features added to the set	Criterion value (Misclassification rate)
Average RBC Thickness (3D-F1)	0.252396
RBC Perimeter (2D-F2)	0.134185
Top view surface area-volume ratio (3D-F4)	0.0670927
sphericity coefficient (3D-F9)	0.0607029
The upper side of the ring divided by lower side of the ring (3D-F11)	0.0511182
Adding next feature to the feature set (6^{th} feature)	0.479233
Adding next feature to the feature set (7^{th} feature)	0.479233
Adding next feature to the feature set (8^{th} feature)	0.479233

According to Table.3.8 after adding 7^{th} and 8^{th} feature, the misclassification rate never changes. It means that they have no contribution to the final feature set. Adding 6^{th} feature decreases the misclassification rate marginally but we still did not consider it as part of the feature set since we wanted to keep the final feature set as small as possible (Only five features). Figure.3.12 shows the data distribution RBCs for each selected feature. We can see that the distribution of average RBC thickness of echino-spherocyte RBCs has almost no overlap with other distributions (Fig 3.12(a)). Table 3.9 shows miss-classification rate of the

final feature-set and PRNN approach.

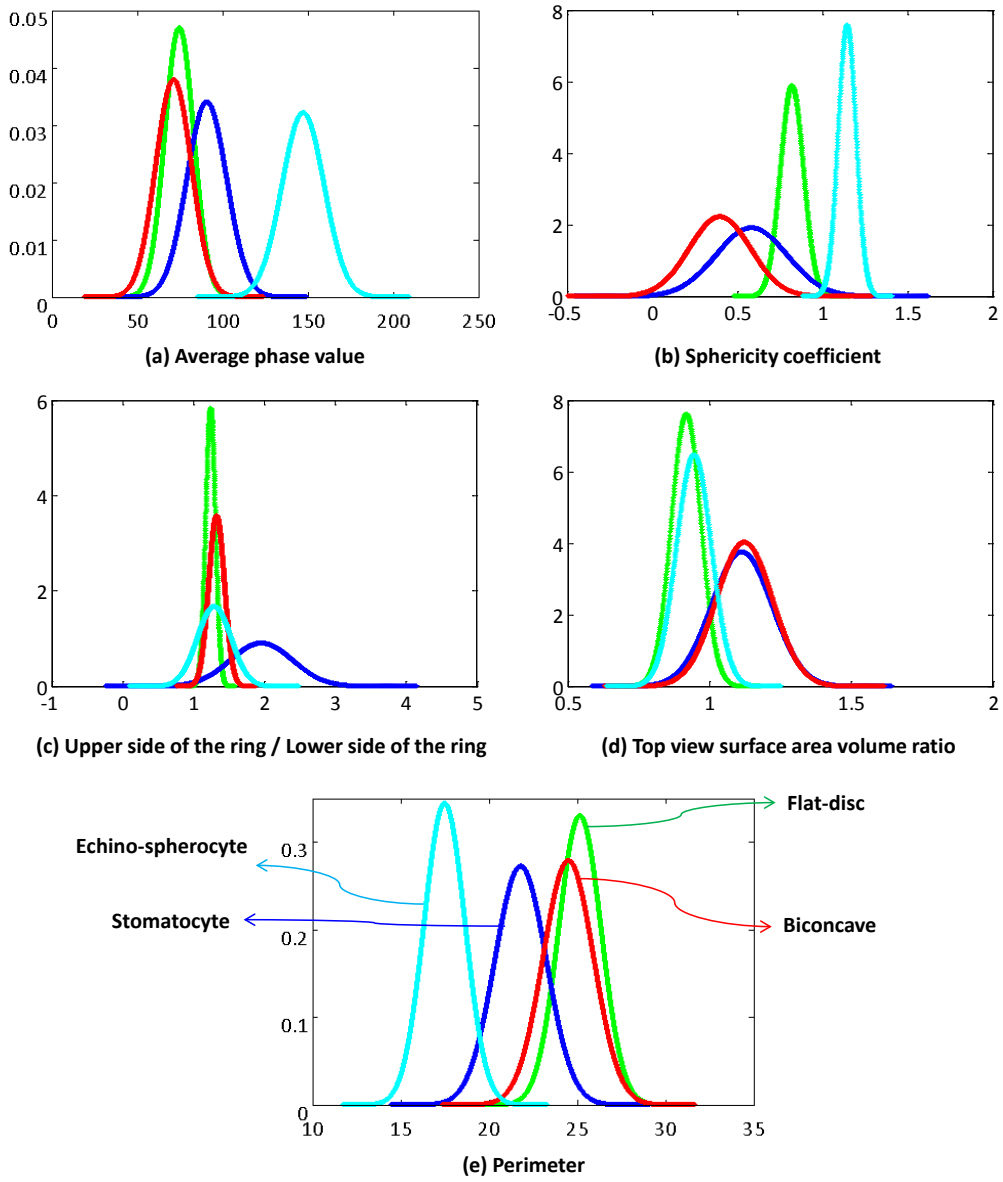

Figure 3.12: Data distribution of the best feature set

Table 3.9: Miss-classification results for the best feature set obtained by sequential features selection

	Flat-disc	Stomatocyte	Biconcave	Echino-spherocyte
Best feature set	**0%**	**0.9%**	**3.1%**	**0%**

The confusion matrix of the test set shows that PRNN sometimes confuses between stomatocytes and echino-spherocytes because there are cases in which RBC has a morphology similar to both stomatocyte and echino-spherocytes (see Fig. 3.13). According to Fig. 3.13 we can see that RBC is similar to both stomatocyte and echino-spherocytes morphology and posterior probability for belonging to stomatocyte and echino-spherocyte category are 0.33 and 0.66, respectively. Even for a human examiner it can be difficult to put it in the correct category.

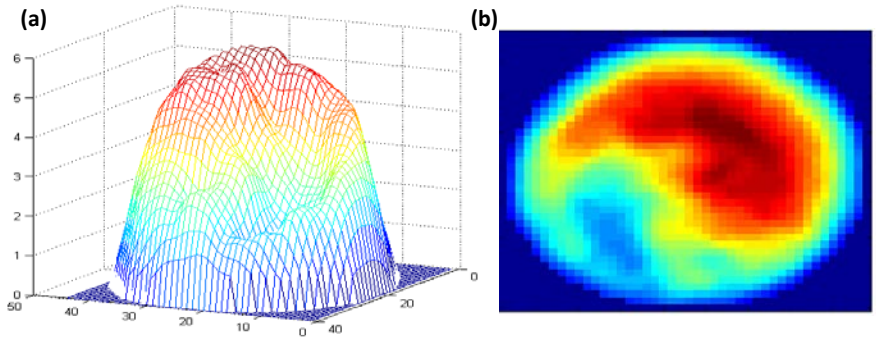

Figure 3.13: A RBC sample that confuses neural network, resemble to both stomato and spherocyte. (a) 3D representation and (b) representation on X-Y plane.

In another experiment, we tried to count different type of RBCs in five quantitative phase images with multiple RBCs. Images are inspected visually by the human inspector and then results are presented. In Fig. 3.14(a) stomatocyte RBCs are dominant (flat discs 0/80, stomatocytes 58/80, biconcave 8/80 and echino-spherocyte 14/80) and in other images biconcave RBCs (Fig. 3.14(b) has following flat discs 2/27, stomatocytes 5/27, biconcave 20/27 and echino-spherocyte 0/27) and echino-spherocytes are dominant (Fig. 3.14(c) has following RBC types of flat-disc 0/49, stomatocytes 5/49, biconcaves 6/49 and echino-

spherocytes 38/49, and Fig. 9(d) has following RBC types of flat-disc 0/63, stomatocytes 3/63, biconcaves 1/63 and echino-spherocytes 59/63). Figure 3.14(e) shows an image with 40 days storage time with many flat-disc RBCs (flat-disc: 16/36, stomatocytes: 7/36, biconcaves: 5/36 and echino-spherocytes: 8/36). The numbers in parenthesis show the number of each morphology obtained by the human inspector. At first, each image is segmented into many RBCs since feature extraction should be applied at the single cell level. Then, the percentage of the different types of RBCs in the RBC phase images is calculated. As expected, the classifier showed that at the first sample stomatocyte RBCs are dominant. In contrast in the second and fifth figure biconcave and flat-disc RBCs are the major types. Third and fourth figures illustrate that echino-spherocytes are dominant RBCs. Although there is a small error in counting non-dominant RBCs, the main and important thing is counting and reporting the dominant type for further investigation.

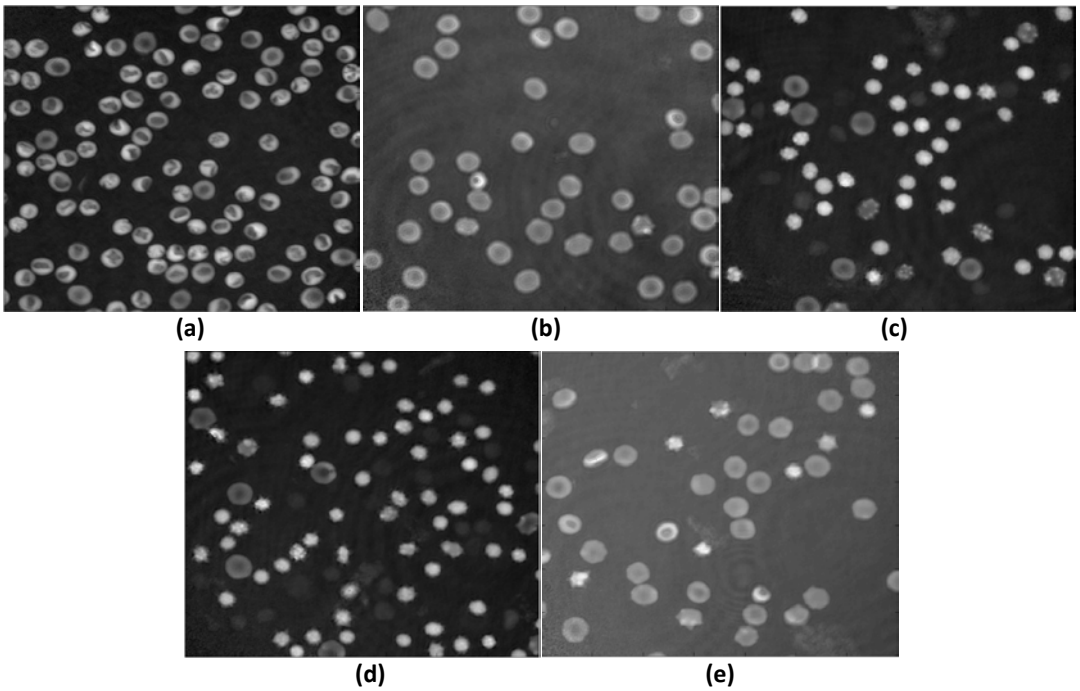

Figure 3.14: Five RBC samples and counting results. (a) Flat-disc: 2.5% (2/80), Stomatocytes: 76.2% (61/80),

Biconcave: 11.25% (9/80) and Echino-spherocyte: 10% (8/80). (b) Flat-disc: 7.40% (2/27), Stomatocytes: 18.51% (5/27), Biconcave: 74.07% (20/27) and Echino-spherocyte: 0%. (c) Flat-disc: 0%, Stomatocytes: 12.24%(6/49), Biconcave: 10.2% (5/49) and Echino-spherocyte: 77.55% (38/49). (d) Flat-disc: 0%, Stomatocytes: 7.94% (5/63), Biconcave: 1.59% (1/63) and Echino-spherocyte: 90.4% (57/63). (e) Flat-disc: 47.22% (17/36), Stomatocytes: 25% (9/36), Biconcave: 19.44% (7/36) and Echino-spherocyte: 8.3% (3/36).

According to the results, the proposed feature set and classifier can automatically count and categorize different types of RBCs in human RBCs by taking advantages of 2D and 3D profile of RBC. The classifier is helpful to assess RBC-related abnormality since the ratio of the different types of RBCs is associated with certain types of diseases. There are some disadvantages in using NN technology regarding the classification such as there is no formula for the number of nodes and hidden layers. Generally, these numbers in the network are problem dependent and are decided by the trial-and-error method.

We believe that DHM, by providing the quantitative phase images, allows for doing different analysis especially classification goals. For example, someone can easily classify echino-echino-spherocyte from the rest of cells easily by using a conventional binary support vector machine (SVM) classifier and one or two features. Figure.3.15(a), for example, shows the density of average cell thickness of echino-spherocytes against other RBCs. Any binary classifier can be used to separate these two groups. Figure.3.15 (b) shows the scattering of two groups based on average thickness value and surface area, and an SVM classifier with its boundary region.

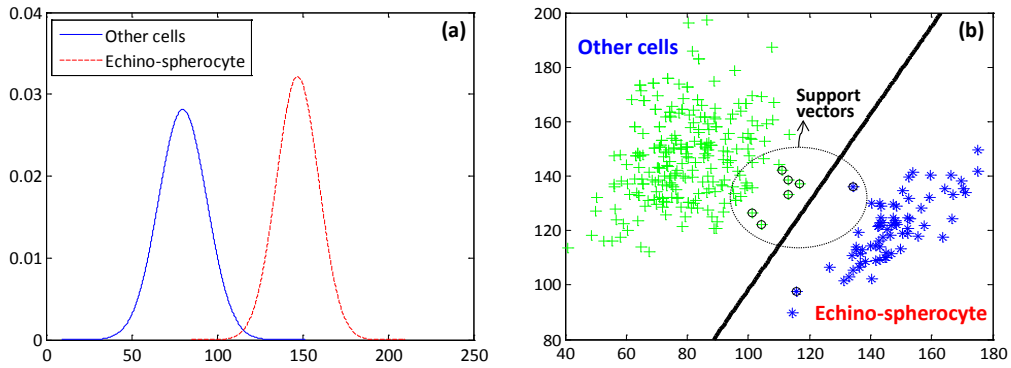

Figure 3.15: (a) average thickness value distribution for echino-spherocytes and other RBCs, (b) an SVM classifier to separate echino-spherocytes and other cells using average thickness and total surface area.

e. Conclusions

Automatic classification of different types of RBCs in human RBC is a challenging and important problem for pathological diagnosis. In particular, as far as RBCs are concerned, classification based on their 3D profile is highly relevant. Another issue is that since demands on laboratories are ever increasing and funding and staffing levels are generally below the desired level, the implementation of a system which shortens staff time, cost-effective and non-invasive is greatly desired. In this research, we have presented and assessed the use of pattern recognition neural network applied to the 2D and 3D features of RBCs obtained through DHM in order to categorize and count biconcave, stomatocyte, flat-disc and echino-stomatocyte RBCs in an RBC sample with multiple types. Six 2D features and thirteen 3D features have been extracted and classification results are compared right after. Our experimental results show that the 3D features have more useful information in RBC classification. In addition, feature selection shows that average RBC thickness, top view surface area volume ratio, sphericity coefficient, the upper side of the ring divided by lower side of the ring and RBC

perimeter can better classify RBCs into the desired categories. The experimental results and the performance imply that the final feature set can help in classifying and counting RBCs which is substantially important in analyzing RBC abnormality and shape-related diseases.

C. Automated quantification of red blood cell fluctuations by time-lapse holographic cell imaging

f. Motivations and introductions:

The functionality of human red blood cells (RBCs) has clinical relevance for hematology and depends on RBC dynamics and morphology. We propose automated methods to quantitatively calculate fluctuations rate with nanometric axial and millisecond temporal sensitivity at the single-cell level by using time-lapse holographic cell imaging. For this quantitative analysis, cell membrane fluctuations (CMFs) were measured for RBCs stored at different storage times. Measurements were taken over the whole membrane for both the ring and dimple sections separately. The measurements show that healthy RBCs that maintain their discocyte shape become stiffer with storage time. The correlation analysis demonstrates a significant negative correlation between CMFs and the sphericity coefficient which characterizes the morphological type of erythrocyte. In addition, we show the correlation results between CMFs and other morphological and chemical properties such as projected surface area, mean hemoglobin content, mean corpuscular volume, and surface area.

g. Introductions and Sample Preparations:

Red blood cells (RBCs) are composed of water, proteins (the most abundant of which is hemoglobin), lipids, and carbohydrates [73]. Mature erythrocytes, which are sometimes also referred to as discocytes, are the main cell type in the blood circulation. Their biconcave shape

is formed by a flexible membrane that allows significant deformation. This configuration has the maximum surface area for a given volume and allows rapid deformations while passing through small capillaries during microcirculation. Such a biconcave shape is assumed to have resulted from the minimization of the free energy of the membrane under area and volume constraints, since there are no complex internal structures within an RBC [33]. RBCs must adapt to a wide range of capillary sizes, and deform while maintaining their cellular integrity and function. This is made possible by the absence of a three-dimensional (3D) cytoskeleton in RBCs. Their shape and mechanical integrity are maintained instead by a two-dimensional (2D) hexagonal lattice formed of flexible spectrin tetramers, which are linked by actin oligomers. Since the side length of actin (70-80 nm) is much smaller than the contour length of a spectrin tetramer (approximately 200 nm), it is believed that spectrins are the principal contributors to the bending of membranes or curvature modulus [74, 75]. Two kinds of effects have been suggested as driving agents of cell-membrane fluctuations (CMFs). The first is thermal motion, which is more prominent in membrane regions with a small curvature (the dimple region). The second is linked to the metabolic activity that determines the ATP content in the membrane skeleton and to the involvement of actin. The second type of fluctuations is believed to happen in regions of high curvature, such as the ring section of RBCs [76].

As mentioned earlier, different factors influence the deformability of RBCs. However, under storage conditions (e.g., in blood banks), RBCs undergo molecular, metabolic, biochemical and biomechanical changes, which are commonly referred to as storage lesions. Briefly, such processes result primarily in a decrease in energy metabolism,2,3 diphosphoglycerate (DPG), adenosine triphosphate (ATP), and nitric oxide.

Furthermore, during storage, the erythrocyte shape alters from deformable discoid to an irreversibly deformed spheroechinocytes. It is due to the irreversible loss of membrane by the formation of vesicles, which is the cause of an increased osmotic fragility [32,38,51,52,77-82]. It is understood that these changes are associated with decreased deformability, poor

functionality of RBC and consequently with the removal of RBCs from the bloodstream [79-82].

One important question is regarding the extent to which the morphological and biochemical changes occurring under storage conditions affect membrane fluctuations. Another question is whether there is any correlation between the dynamic and static parameters. In order to address these questions, we propose automated methods for measuring quantitative fluctuations rate at the single-RBC level as a function of their storage time, using time-lapse digital holographic imaging. We also analyze both the ring and dimple regions of the cell separately, since we believe that fluctuations have different causes. Images were acquired every few days over a 71-day period to investigate the quantitative alterations of RBC parameters over storage time systematically. The erythrocyte concentrate (EC) from which the RBC samples were collected were prepared at the blood center of the *Transfusion Interrégionale CRS* (Epalinges, Switzerland) as follow: 450±50 mL of whole blood were collected and mixed with 63 mL citrate-phosphate-dextrose (CPD) anticoagulant. The bags were centrifuged to separate blood components. Then, semi-automated pressure applied to distribute the blood fractions into sterile inter-connected blood bags (Fenwal, Lake Zurich, IL, USA). Finally, to remove residual leukocytes the erythrocytes were filtered and 100 mL of saline-adenine-glucose-mannitol (SAGM) additive solution were added. Five mL of each sample were collected using a sampling site weekly during 71 days (the 4 ECs were stored at 4 °C) [83]. To prepare the RBCs, the EC samples were washed two times with NaCl 0.9% (centrifugation at 2000 g, during 10 min at 4°C) and resuspended in HEPA 10 mM glucose. The RBCs were then seeded in a 96-well plate coated with poly-L-Ornithine for image acquisition.

The static morphological properties (mean corpuscular volume (MCV), projected surface area (PSA), surface area, and sphericity coefficient) and mean hemoglobin content (MCH) at the single-RBC level were measured. Having measured the fluctuations rate and the morphological and biochemical changes, we calculated the correlation of these parameters to the fluctuations rates at different times. Since previous studies mentioned that the RBC morphology affects

stiffness [75, 80], the present study focuses exclusively on biconcave RBCs. Additional reasons include that such cells are convenient for discrimination between the ring and dimple sections. Our quantitative analysis reveals some interesting points. First, we demonstrate that older cells (71 days storage) that have preserved their original discocytic shape are a little bit stiffer than younger ones (stored for 4 days). Also, the fluctuations rate in the dimple is greater than in the ring section in younger RBCs. The MCV, MCH, PSA, and surface area do not change significantly on these time scales. Interestingly, we show that the CMFs of a whole cell (for cells stored for 4 days) show significant negative correlation with the sphericity coefficient which means that more spherocyte cell becomes, less fluctuations it can have. A significant positive correlation between the dimple fluctuations and the sphericity coefficient is also observed. Membrane Fluctuations rate (methods and approaches)

Different techniques have been proposed to measure fluctuations in RBC membranes [74-76, 80]. However, their separate applications to the ring and dimple sections remain to be carried out, since we believe that the sources of their fluctuations are different. To calculate the fluctuations rate, we consider the statistical model of Rappaz et al. [76]. Briefly, this requires the definition of a region of interest (ROI) and two independent variables: $std(h_{cell}+h_{background})$, the temporal deviation within the RBC area (combining both the cell fluctuations and noise), and $std(h_{background})$, the mean temporal deviation calculated over all the pixels located outside the RBC area (see Fig. 3.16). The measured standard deviations (see Fig. 3.17) for one pixel outside the cell (point “A”), on the ring (point “B”) and at the center (point “C”), are 17, 42 and 29 nm, respectively, indicating that the membrane fluctuation amplitudes are significantly larger than the background noise level (see Fig. 3.17). Accordingly, the fluctuations at each single pixel $CMF(x,y)$ can be evaluated as [76]:

$$CMF_{cell}(x,y) = \left[\left(std\left(h_{cell}+h_{background}\right)(x,y)\right)^2-\left(std\left(h_{background}\right)\right)^2\right]^{1/2}. \quad (19)$$

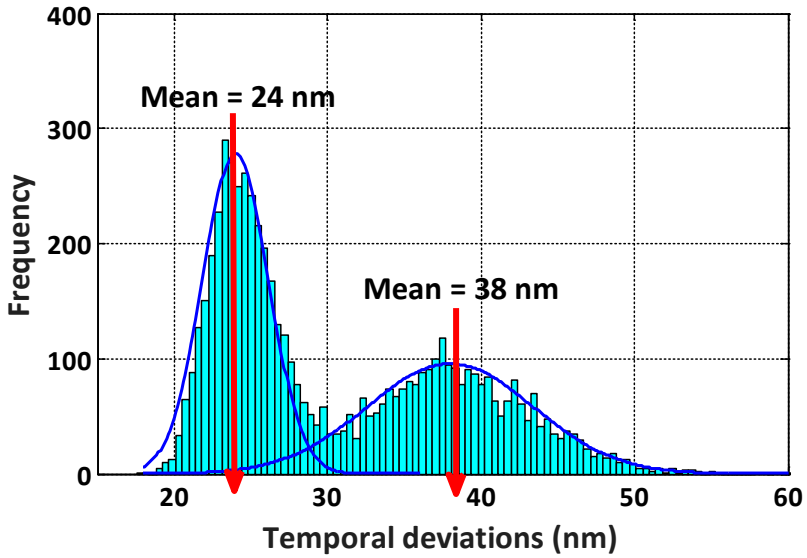

Figure 3.16: Distribution of temporal deviations within a ROI; the left-side distribution represents the background and the right side corresponds to the membrane and noise.

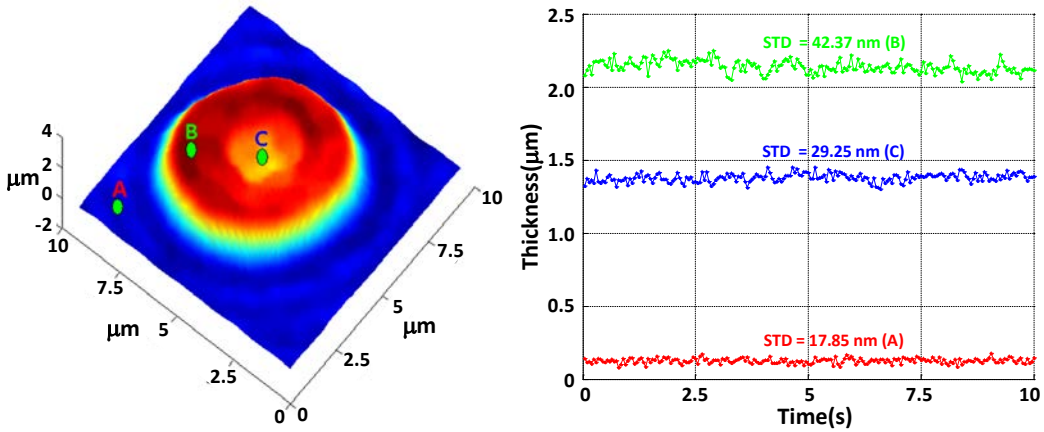

Figure 3.17: Thickness signals in three different regions recorded at 20 Hz over a 10s period ("A" denotes a background location, "B" is on the cell ring, and "C" is in the dimple region). The standard deviations of the signal are 17, 42, and 29 nm, respectively.

Several strategies can also reduce noise effects. A temporal summation of three images and a median filter with size 5×5 pixels were utilized. It can also be noted that an RBC occasionally displays significant lateral displacements in time-lapse sequences. The lateral movement of RBCs, which are in the process of becoming spherocytes, could be caused by the loose attachment of the cell to the substrate (only a small portion of the membrane is in contact with the substrate). Such cases also display strong changes in CMFs. We canceled these lateral displacements by utilizing the *ImageJ*[84] software and the *StackReg*[85] plugin. Another concern is the steep membrane gradient at the cell border and around the center of the cell, where a small lateral displacement of the cell membrane has a strong impact on the OPD value, since the OPD measures variations in thickness along the *z*-axis (blue vector in Fig. 3.18(b)). In order to avoid systematically overestimating cell fluctuations in such steep-slope regions, cell fluctuations must be evaluated in a direction perpendicular (normal) to the cell membrane (green vectors in Figs. Fig. 3.18 (a) and (b)). Finally, normal fluctuations can be estimated as:

$$h_n(x,y) = h(x,y) \times \cos(\theta_{(x,y)}). \tag{20}$$

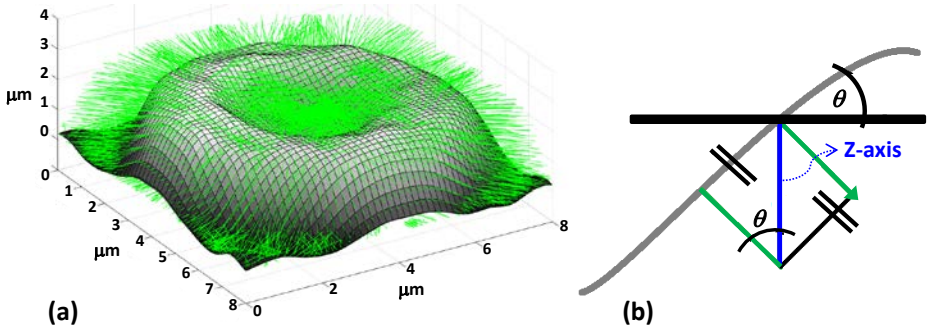

Figure 3.18: (a) RBC mesh with normal vectors. (b) X-Z view of the membrane surface and its normal vector.

During our experiments, we realized that RBCs sometimes undergo lateral movements (i.e., in the X and Y directions), particularly cells that have started suffering the echinocytic process (with a sphericity coefficient close to 1) [see Fig. 3.19].

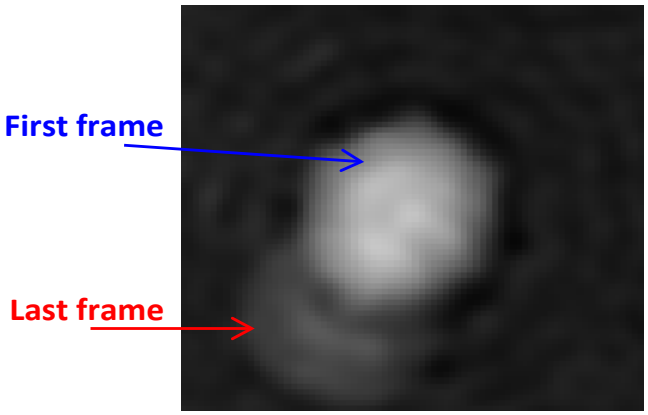

Figure 3.19: A sample RBC undergoing a spatial displacement. The first and last frames are blended (the first frame is made less opaque than the last frame to facilitate visualization).

As mentioned, we used the *Imagej* software and the *Stackreg* plugin. However, we found that even small displacements can produce large changes in the fluctuations rates, particularly at the edges of the cell. We therefore adopted another strategy to isolate the cells from the background area. First, we applied a thresholding procedure involving the simplest and most basic image segmentation algorithm:

$$I'(x,y) = \begin{cases} 0 & I(x,y) \le T \\ 1 & I(x,y) > T \end{cases}, \tag{21}$$

where T (here set to 0.35) is the threshold value, and $I'(x,y)$ and $I(x,y)$ are the intensity values in the segmented and original images, respectively. The above equation generates two masks that can be used to discriminate between the cell and background areas. In order to ensure that a cell is properly isolated, we "eroded" the background mask by a few microns. The erosion of the binary image I' by the structuring element S is defined by

$$I' \Theta S = \{ z \mid S_z \subseteq A \}, \tag{22}$$

where S_z is the translation of S by the vector z. Simply put, the erosion of I' by S can be understood as the locus of points reached by the center of S when it moves inside I'. Here, the structuring element is a flat disk of approximate radius 0.5 mm (see Fig. 3.20).

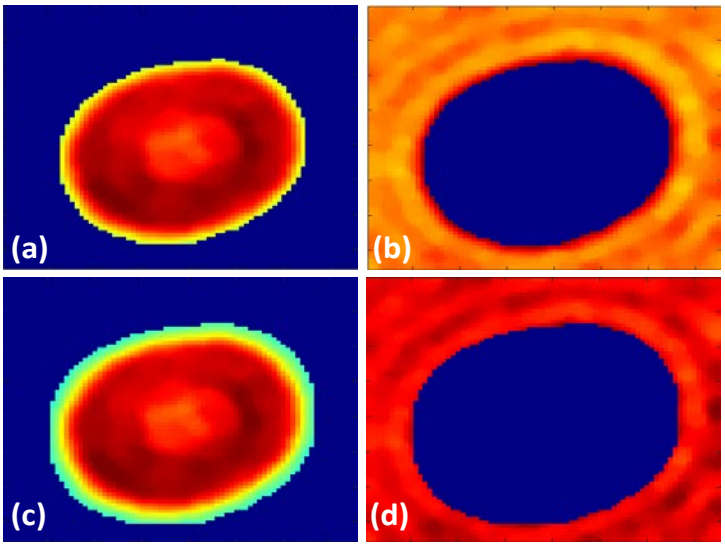

Figure 3.20: (a) RBC after thresholding, (b) background after thresholding, (c) RBC after background erosion, and (d) eroded background area

Figure 3.22 shows a deviation map of the ring, central, and background regions. Biconcave and

spherocyte cells are separated systemically using sphericity coefficients (stomatocytes are removed manually from the biconcave set). The method used to discriminate biconcave cells from cells with other morphologies is as following. We found that the sphericity coefficient can be very helpful in this regard. The sphericity coefficient k is the ratio of the RBC thickness h_c at the cell center to the thickness h_t at a radius that is halfway to the cell perimeter:

$$k = \frac{h_c}{h_t}. \tag{23}$$

This metric can distinguish between three types of RBCs. A value of k less than 1 characterizes a biconcave RBC, a value close to 1 denotes a flat disk, and a value greater than 1 tends to a spherocyte. In this work, a threshold value of $k_t = 0.97$ is assigned to distinguish biconcave cells from spherocytes and echinocytes. The procedure is simple and efficient. After making two masks to isolate the cell and background as described earlier, we calculate the projected surface area (PSA) of the cell. The cell radius can then be evaluated as:

$$r \cong \left(\frac{PSA}{\pi}\right)^{1/2}. \tag{24}$$

Using r, we can select candidate pixels that are likely to lie near the ring section. Since the above procedure cannot precisely identify the points located exactly on the ring section, we search for the pixel with the greatest thickness value in the vicinity of each candidate pixel (within a region of size 3 pixels by 3 pixels). Finally, we define h_t as the arithmetic average of the heights of all these corrected points (red points in Fig. 3.21).

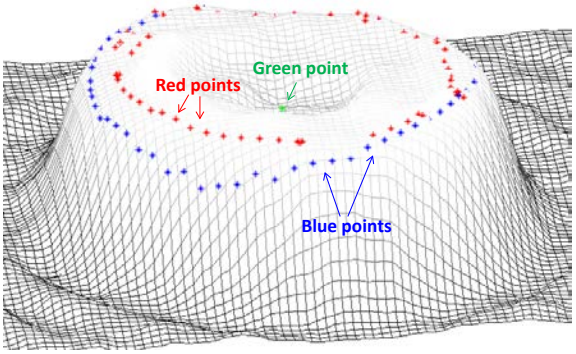

Figure 3.21: Blue points show the points obtained by using *r*. The red points identify the maximum values within a range of 3 pixels from the blue points. The green point shows the geometric center of the cell.

It turns out that the CMFs of the whole membrane, ring, and dimple are 35±4.7 (n = 33; RBC age is 4 days)(in agreement with previously reported values [76, 86]), 35±5.2, and 36±5.3 nm, respectively (see Fig. 3.22).

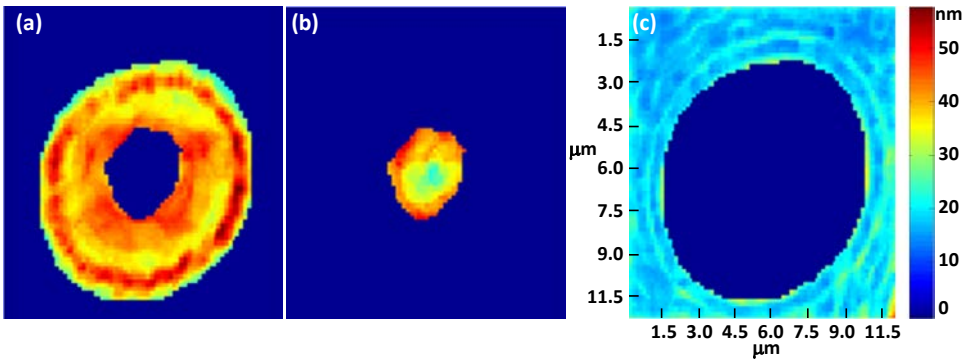

Figure 3.22: Deviation map of (a) the ring and (b) dimple sections of a RBC, and (c) the background (after 4 day of storage). Color-bar scale has units of nanometers.

h. Quantitative Analysis of RBC Fluctuations

In the present work, numbers written after a ± sign denote a standard deviation (STD). In our correlation analysis, we calculated the Pearson product-moment correlation coefficient and adopted a 95% confidence level when applying the *t*-test method. Error bars shown in the plots represent twice the

corresponding standard deviations. After calculating the fluctuations rates, morphological parameters, and the MCH for different storage times, we can monitor the impact of storage lesions on the RBC fluctuations rate and 3D structure. In this study, more than 33 RBCs were extracted from each image (4 ECs) to measure the parameters. As mentioned earlier, we measured the RBC volume using a Sysmex analyzer for the purpose of results confirmation. In addition, the MCH was measured with the same tool to confirm consistency with the MCH obtained by DHM. After calculating the morphological parameters, we realized that the RBC volume fluctuated around its average value, in the range 84±10 to 87±8.8 μm^3 for the RBCs stored between 4 and 71 days. Our values agree with previous reports [22-23]. We also found a small increase in the sphericity coefficient, signifying that the cells are becoming more spherical, less deformable, and stiffer, which arguably also affects the fluctuations rate. The sphericity coefficient increases from 0.74±0.09 in young cells (stored for 4 days) to 0.79±0.12 in older cells (stored for 71 days), consistent with reported values [23]. In the case of older RBCs, the STD value of the sphericity coefficient is significantly larger (±0.12). We believe that this results from biconcave cells gradually becoming spherical. The MCH does not change and only fluctuates around its average value of 32±0.6 pg (See Fig. 3.23), consistent with earlier reports [75, 22-23] and MCH is in agreement with the chemical experiment in the present study (Fig. 3.23). This constancy indicates that, while biconcave RBCs undergo small changes during storage, they do not leak hemoglobin into the storage solution [75, 80].

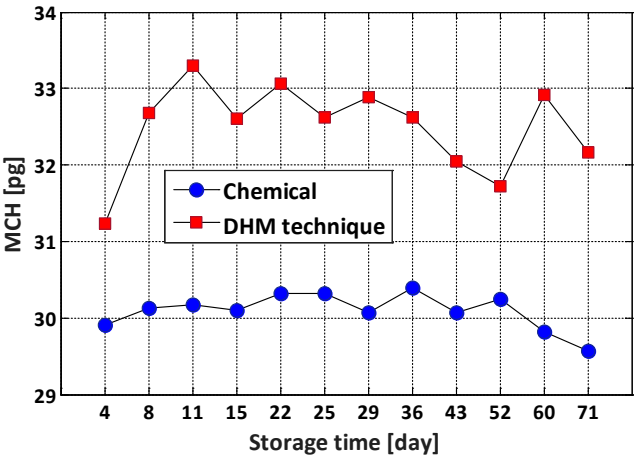

Figure 3.23: MCH changes versus storage time

The CMF rate fluctuates over the storage time. However, the general trend of the whole RBC, the ring, and the center is to decrease with storage time (F-statistics suggest that the linear regression line has a slope that is significantly different from zero; p-value <0.05), consistent with earlier findings [75]. Our experimental results show that RBC membranes stiffen with storage time, in agreement with the reported decrease in deformability [75, 79, 80, 87]. According to Fig. 3.24, fluctuations at the dimple are generally larger than in the ring region ($p<0.05$; two-sample Kolmogorov-Smirnov test), as expected and in agreement with the results of Rappaz et al. [76] (Age of RBC is 4 days). Figure 3.25 shows the correlation analyses of the fluctuations rate of young RBCs (stored for 4 days; n = 33) with the morphological and biochemical parameters of both the membrane and the dimple section. The ring section follows the same trend as the whole membrane. We therefore decided to exclude ring-section results from our correlation analysis results shown in Fig. 3.25. Interestingly, the membrane fluctuations exhibit a strong negative correlation with the sphericity coefficient ($p<0.05$; Pearson product-moment correlation test). The greater k is, the fluctuations are fewer in the membrane. This can be simply understood from the fact that the more spherical RBCs is, the stiffer it becomes [79, 87]. On the other hand, there is a significant positive correlation between the fluctuations rate in the dimple region and the k factor (Fig. 3.25(a)). The lower the PSA of a RBC, the larger the observed membrane fluctuations (Fig.

3.25(b)). Whole membrane and dimple fluctuations (Fig. 3.25(c)) have no significant correlation with the MCH, consistent with previous findings [75, 35]. Figure 3.25(d) and 3.25(e) shows that membrane fluctuations are not correlated with the MCV and surface area value (We also evaluated the correlation between the CMF and static morphological parameters of RBC for two storage times of 43 and 71 days. The results are not shown here).

Our statistical model for evaluating fluctuations rates suggests that the fluctuations rates in discocyte RBCs and in both the ring and dimple regions differs between young and old RBCs. Indeed, our results reveal that the MCH does not vary with storage time, which means that the total dry mass of a cell remains constant over time [75]. Further, the constancy of the PSA during blood banking shows a tendency of biconcave RBCs to maintain their general structure.

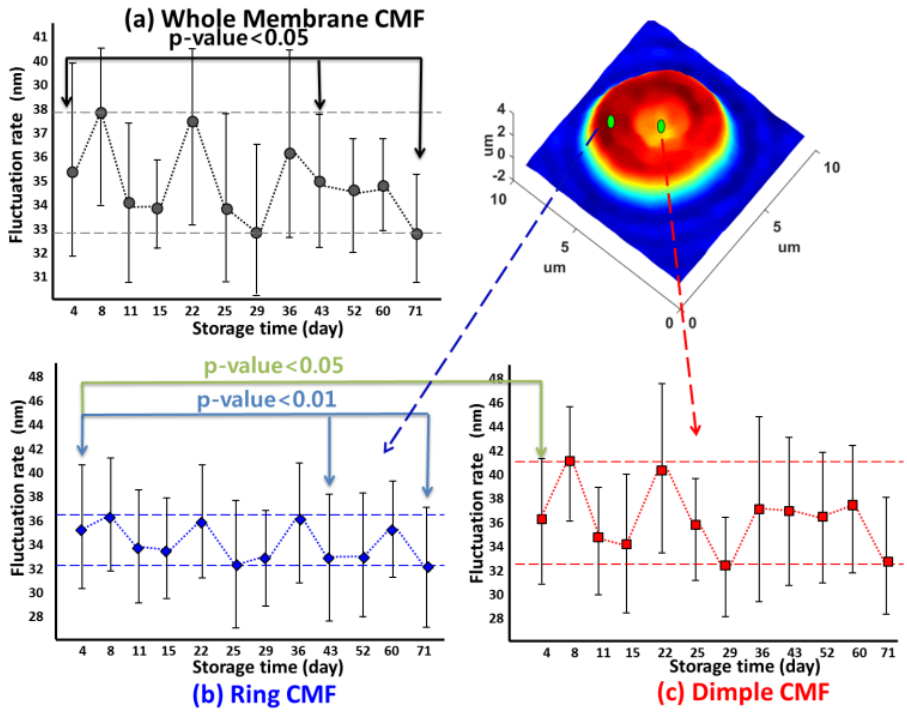

Figure 3.24: Evolution of fluctuations rate over storage time for (a) the whole membrane, (b) the ring, and (c) the dimple region. The length of the error bars measures two standard deviations (Statistical test is Two-sample Kolmogorov-Smirnov test; $p<0.05$ is considered as significant).

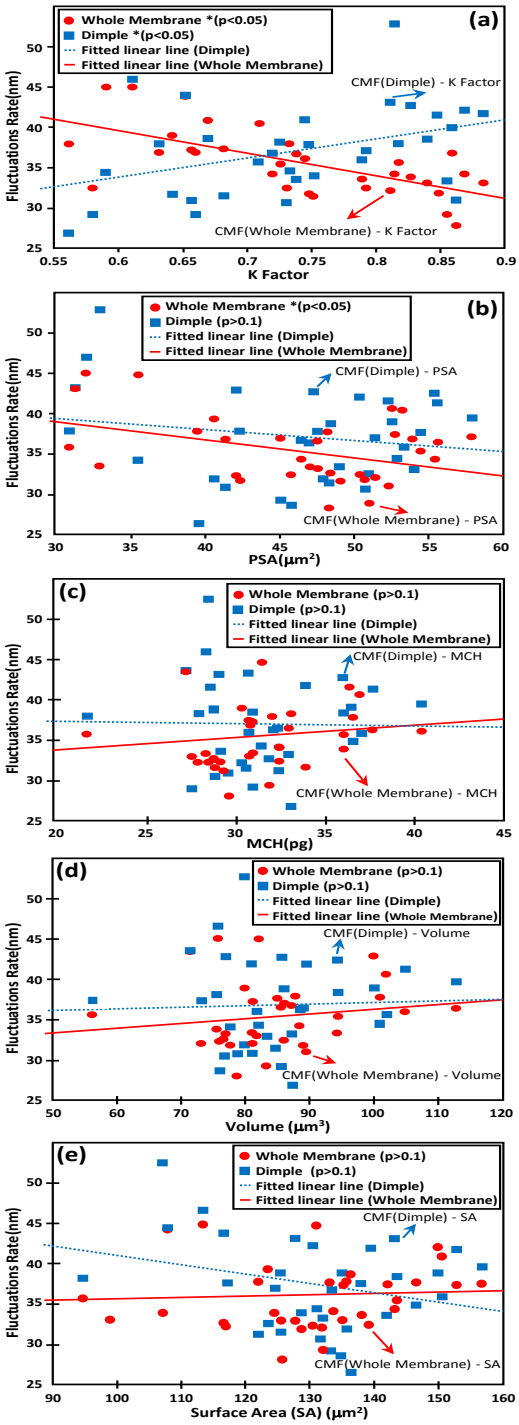

Figure 3.25: Correlation measurements between the fluctuation rate and the morphological and chemical

parameters, for the entire membrane and the dimple region of discocyte RBCs. (a) sphericity coefficient, (b) PSA, (c) MCH, (d) MCV, and (e) surface area. Storage time is 4 days and n=33. (An asterisk * indicates a significant linear correlation by Pearson p<0.05).

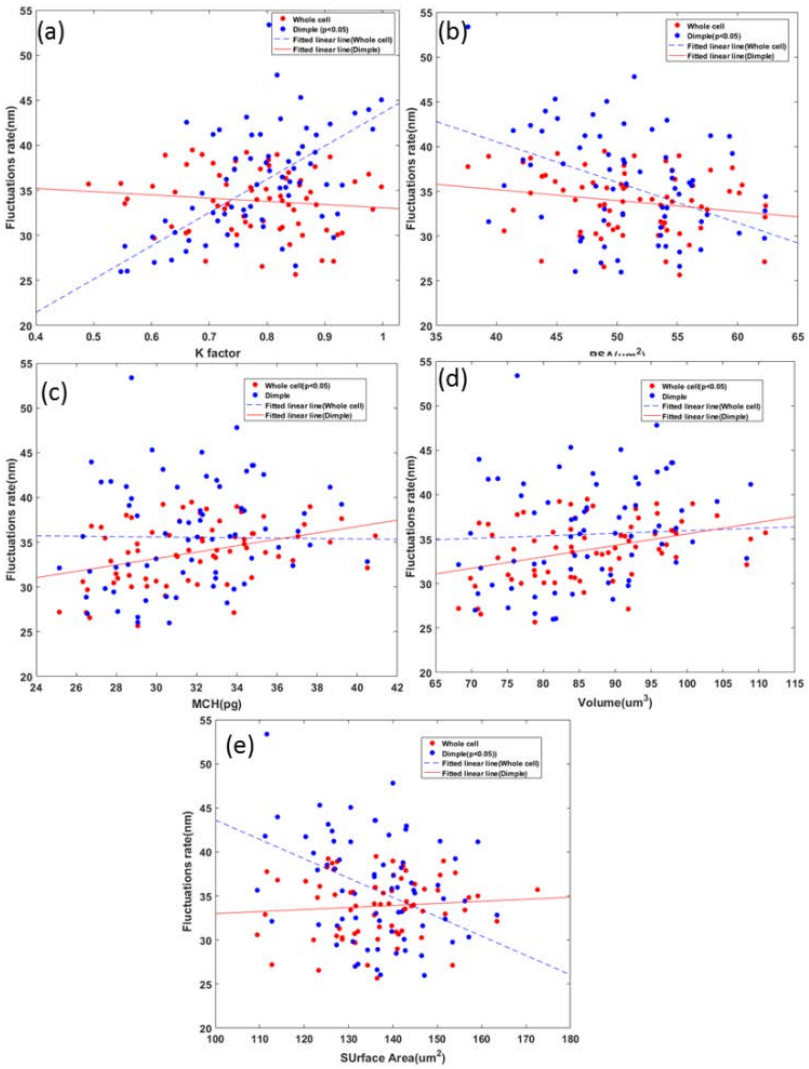

Figure 3.26:Correlation measurements between the fluctuation rate and the morphological and chemical parameters, for the entire membrane and the dimple region of discocyte RBCs. (a) sphericity coefficient, (b) PSA, (c) MCH, (d) MCV, and (e) surface area. Storage ti

During circulation, normal RBCs must deform to penetrate capillaries with a diameter almost half

the size of a typical RBC. Their resistance to deformation may not, therefore, be substantial but not too small either, lest it compromise the integrity of the cell in normal circulation [88]. Previous experiments [75, 79, 80, 86, 87] have revealed that RBCs become less deformable and much stiffer over longer storage periods. The consequences are significant and potentially seriously detrimental to human organs. It is more difficult, if not impossible, for stiff RBCs to traverse a microcapillary system. Obstructed capillaries cause pain and damage to tissues and organs. Longer transit times through capillaries, resulting from lower RBC deformability, can also hinder oxygen delivery and carbon-dioxide absorption. This increase in stiffness with the aging of the RBC can be explained in several ways. The membrane area is reduced due to the release of microvesicles [89]. Also, ATP is crucial for preserving the biconcave shape, as shown in chemical experiments where the depletion of ATP caused a change from the biconcave to the echinocyte shape and finally yielded a spherocyte. This change of shape suggests that ATP and membrane loss stiffen the cytoskeleton and hence constrains the bilayer to a smaller cytoskeleton-projected area. The underlying physical origin of this effect is the change in the number of released spectrin filaments with the reduction in the number of defects as the ATP concentration is reduced [86-90]. Interestingly, it has been shown that the ATP concentration in RBCs decreases with increasing RBC age, or near the end of the RBC lifespan [91]. It is presumed that lower ATP concentrations linked to increasing age should correspond to a denser cytoskeleton, a higher shear modulus, and a drop in fluctuations rate [90]. Figure 3.27 shows two different RBCs, imaged after different storage times. Figure 3.27(a) displays a smaller sphericity coefficient and larger fluctuations rate. In contrast, the other cell has a greater sphericity coefficient and a smaller fluctuations rate (See Fig. 3.27(b)).

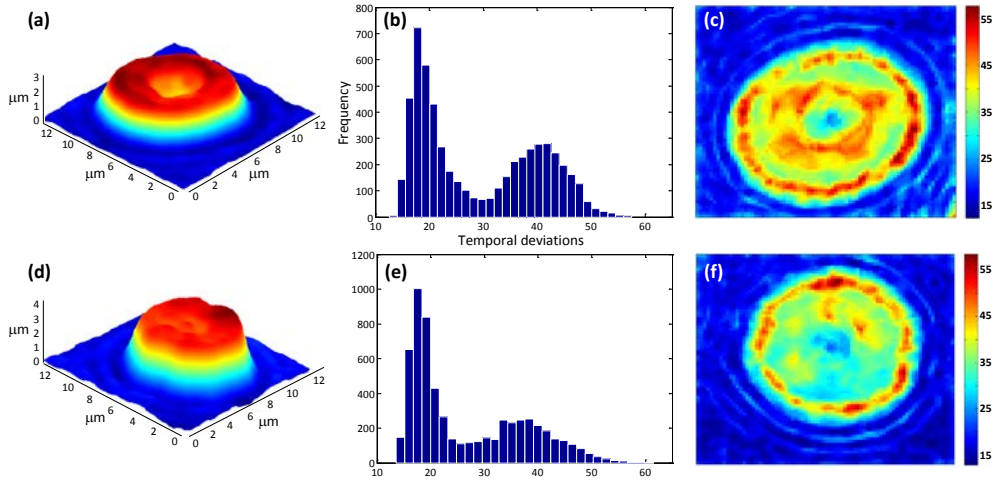

Figure 3.27: 3D reconstruction of a RBC (age 4 days) with k = 0.85, (b) deviation distribution and (c) fluctuation map (average over the whole surface is 34.78 nm); (d) 3D reconstruction of a RBC (age 71 days) with k = 0.95, (e) deviation distribution and (f) fluctuation map (average over the whole surface is 26.33 nm). Color-bar scales are in nanometers

The introduced method is not limited to a specific morphology and can be used in different cases. For example, fluctuations map of different morphologies are obtained and presented in Fig.3.28.

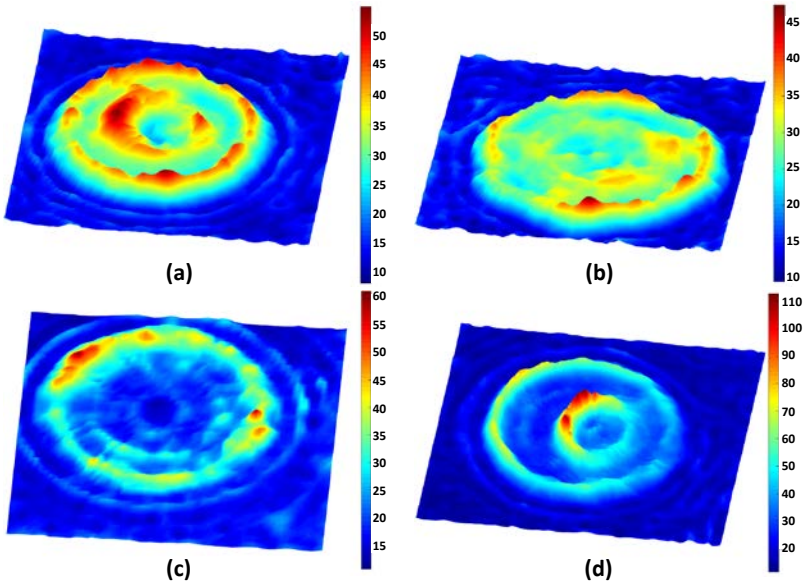

Figure 3.28: Deviation maps for a (a) biconcave (CMF = 30.3 nm), (b) echinocyte (CMF = 25.9 nm), (c) spherocyte (CMF = 23.2 nm), and (d) stomatocyte (CMF = 39.7 nm) RBCs (color-bar scales are in nanometers).

i. Conclusions:

In this study, we quantified fluctuations in the RBC membrane, dimple, and ring in the case of storage lesion using quantitative phase images acquired by DHM. We considered only discocyte cells, which are believed to be more robust under blood-banking conditions or were younger at the time of donation. Since DHM is capable of imaging cells at the single-cell level, we also evaluated morphological properties of the RBC. Interestingly, the fluctuations rate for the membrane and in the ring and central regions decrease with the age of the RBCs. Indeed, we found that the sphericity coefficient of a cell increases with storage time. The decrease in CMF and the increase in sphericity coefficient of the monitored biconcave RBCs imply that RBCs stiffen as they age. The decrease of deformability during storage can have negative impact on transfusion efficiency since perfusion of oxygen to organs is impaired. In addition, our correlation analysis revealed that membrane fluctuations are significantly

correlated with the sphericity coefficient of the monitored biconcave RBCs. We believe the present method will be useful in quantitative clinical applications for hematology targets, since DHM is a label-free non-perturbing imaging method and blood smears can be considered for further investigation.

4 Automated analysis of Controlled and Drug Treated Cardiac Action Measurement Using Digital Holographic Microscopy

a. Motivations:

The primary function of the heart is to pump blood efficiently by virtue of an orchestrated contraction–relaxation cycle of the working cardio muscles or so-called cardiomyocytes (myocardiocytes). The human heart contains an estimated 2 to 3 billion cardiomyocytes cells. By coordinated contraction, these cells control blood flow through the blood vessels of the circulatory system. During the cardiomyocyte contraction, the whole cell changes its 3D shape rapidly, with meaningful intermediate events taking place on the short intervals (milliseconds) [41]. Also, the beating attributes such as beating frequency and peak changes are related to the cellular response to various stimuli and also to differentiation/maturation status. Cardiomyocytes respond to drugs and naturally occurring hormones and it alters the heart-beat rate. Drug development requires the testing of new chemical entities for adverse effects. Adverse drug side effects, such as cardiotoxicity is a major concern in drug development and a major cause of drug withdrawal from the market [42]. Therefore, safety assessments should be performed during drug development to see the possible side effects of the drug; especially those ones which interfere with the well-choreographed and elaborate movement of ions across cardiomyocytes membrane disrupting the electrical activity and beating of the heart [43]. Accordingly, pharmaceutical companies and researchers should ensure that the effects of lead candidate compounds on cardiac function strictly satisfy safety criteria. Therefore, it is highly important to establish more quantitative examination during drug developments and its effects on cardiomyocytes *in vitro* using data analysis algorithms for preventing late stage failure [42].

Most of the biological cells, as well as cardiomyocytes, are transparent or semi-transparent thus the amplitude of the light which interacts with them is minimally affected. Therefore, it is hard to quantitatively examine images of these cells obtained by conventional 2D intensity-based light microscopy techniques. On the other hand, transparent specimens generally alter or shift the phase of light more significantly. Therefore, imaging techniques measuring changes in the phase of light like digital holographic microscopy (DHM) can quantitatively visualize the 3D shape of those cells in non-invasive manner. Analyzing tissues and cells in non-invasive approaches provides a powerful alternative to traditional techniques requiring invasive analysis of studied cells, which may end up to misleading results. DHM is capable of capturing the entire complex field distribution associated with the specimen in a single digital camera exposure, without the need for scanning or contrast agents. This parameter is directly related to the dry mass of the sample [20, 49], therefore, valuable information regarding the morphology and quantitative redistribution of materials within the cardiomyocytes can be obtained. DHM has been used in analyzing various types of cells, such as protozoa, bacteria, plant cells, blood cells, nerve cells, stem cells and cardiomyocytes. DHM is especially useful for acquiring fast cell dynamics, such as the red blood cell fluctuations or spatial transients occurring during the contraction of cardiomyocytes [41, 42].

In this work, we analyze changes of parameters of E-4031 drug-treated and controlled cardiomyocytes with high spatial and temporal resolution. We believe that our method is useful in analyzing drug-treated cardiomyocytes and clinical experiments *in vitro* in a label-free manner. The rest of the section is organized as following: In Section “b” we will briefly explain about the material and methods. Section “c” is allocated for the cardiomyocyte dynamic measurements. Section “d” addresses the results and discussions. Finally, Section “e” is the conclusion part.

b. Materials and Methods

Cell preparation:

iCell cardiomyocytes (human induced pluripotent stem (iPS) cell-derived cardiomyocytes) obtained for Cellular Dynamics Int. (Madison, WI) were culture according to the manufacturer's indication and grown for 14 days before recording. Measurements were achieved in a Chamlide WP incubator system for 96-well plate (LCI, South Korea) set at 37°/5% C02 with high humidity.

To obtain images from cardio cells, the coherent laser source with wavelength of λ = 684.5 *nm* is divided into object and reference beam using beam splitter. The object beam illuminates the specimen and creates the object wave front. A microscope objective collects and magnifies the object wave-front, and the object and reference wave fronts are joined by a beam collector to create the hologram. At the end point interfrograms are recorded by a CCD camera and the data is transmitted to a PC for numerical reconstruction algorithms. The quantitative phase images are related to the optical path difference (OPD), expressed in terms of physical properties as:

$$OPD(x,y) = d(x,y) \times \left[n_c(x,y) - n_m \right], \quad (1)$$

In which $d(x,y)$ denotes the cell thickness, $n_c(x,y)$ is the mean intracellular refractive index integrated along the optical axis at the (x,y) position and n_m is the refractive index of the surrounding culture medium. Simply put, Eq. (1) means that the OPD signal is proportional to both the cell thickness and the intracellular refractive index, a property linked to the protein and water content of the cells [20, 49]. DHM have been used in analyzing different parameters of live cells, for example surface area and volume which is based on thickness not OPD value. Converting OPD values to thickness values requires knowing refractive index of the specimen and the surrounding medium. It has been shown that for certain cells, such as red blood cells, in

which a constant refractive index can be assumed for the entire cell contents, the thickness profile can be directly obtained from the phase profile or OPD profile [21]. However, it is limited to homogenous cell types that contain no nuclei or other organelles with varying refractive indices. Although useful morphological parameters including cell surface area and cell volume are based on the thickness profile of the cell rather than OPD value, it has been shown that still OPD can be used to evaluate beating profile of cardiomyocytes and fluctuations of red blood cell membrane [41, 42].

OPD images were acquired by off-axis DHM configuration on a commercially available DHM T-1001 from LynceeTec SA (Lausanne, Switzerland) equipped with a motorized x-y stage (Märzhäuser Wetzlar GmbH & Co. KG, Wetzlar, Germany, ref. S429). Images were recorded using a Leica 20×0.4 NA objective (Leica Microsystems GmbH, Wetzlar, Germany, ref. 11566049). Time-lapse images were for 60 seconds at a sampling frequency of 10 Hz. In total, 600 images are provided. Fig.4.1 shows a cardiomyocyte in two states of minimum peak and maximum peak. Fig.4.2 shows a single cardiomyocyte in two states of minimum peak and maximum peak.

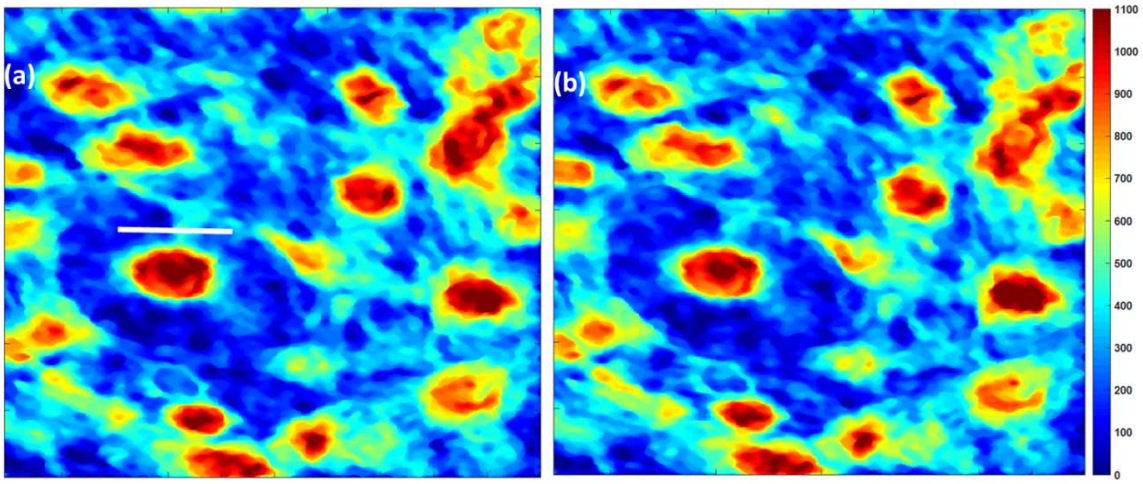

Figure 4.1: Cardiomyocytes at two states (a) maximum of a peak and (b) minimum of a peak. Color bar is similar for both images (nm). White bar is 20 µm.

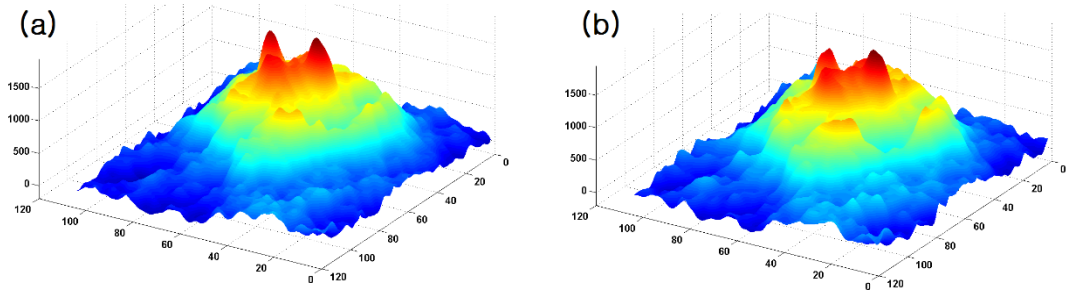

Figure 4.2: 3D representation of a single cell, (a) at the minimum state, (b) at its maximum.

c. Cardiomyocytes dynamics measurement

Several image processing techniques are used in this paper to obtain the dynamic parameters of controlled and E-4031 drug treated cardiomyocyte. The method to obtain beating profile is similar to the published paper by Rappaz [42] with changes to enhance the accuracy of the measurement. Simply put, temporal images are arithmetically averaged and then each image is subtracted from the temporal average. Then, the variance of the subtracted signal is

the cardio beating over the time. The evaluation can be explained by the following equation:

$$\overline{OPD} = \frac{\sum_{n=1}^{N} OPD_n}{N}, \tag{2}$$

$$OPD_h^t = \mathrm{var}\left[OPD(x,y)^n - \overline{OPD} \right], \tag{3}$$

Where OPD_n is the "n"th OPD image from the N samples (N is 600 here). Fig.4.3 shows the beating profile of a controlled cardiomyocytes after utilizing Eq.2 and Eq.3. The obtained variance clearly represents the cardiac action potential. To reduce the noise of the images, a median filter with size of 3×3 pixels is applied to each single image.

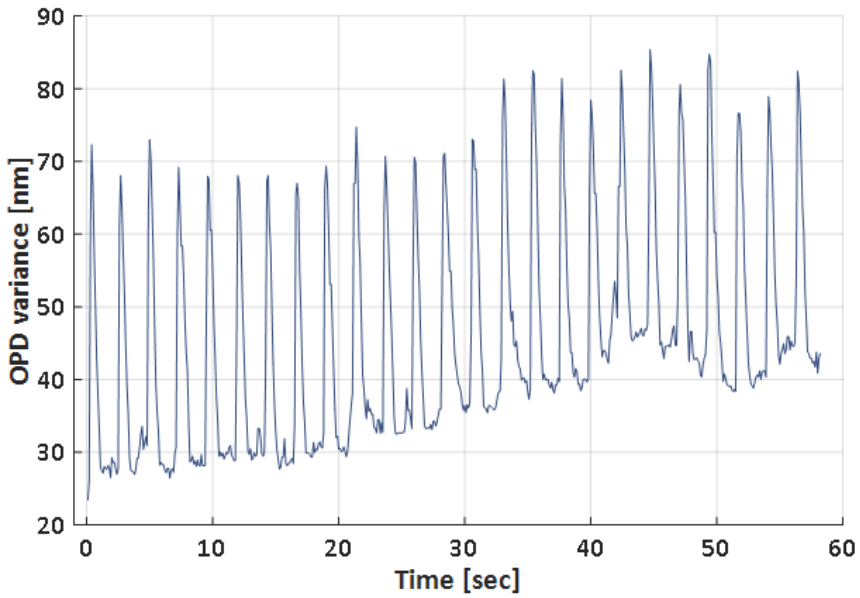

Figure 4.3: Beating profile of a controlled cardio sample

As it has been mentioned before, we utilized new techniques to adopt the algorithm for evaluating dynamic parameters of low beat-rate samples. The first change is that we removed high frequency noise by applying Fourier transformation on the OPD_h signal. In this case, Fourier transform is applied and then high frequency components are removed (Frequencies between 9 Hz and 10Hz). Then, by applying Inverse Fourier Transform the signal is converted

back to the original domain again.

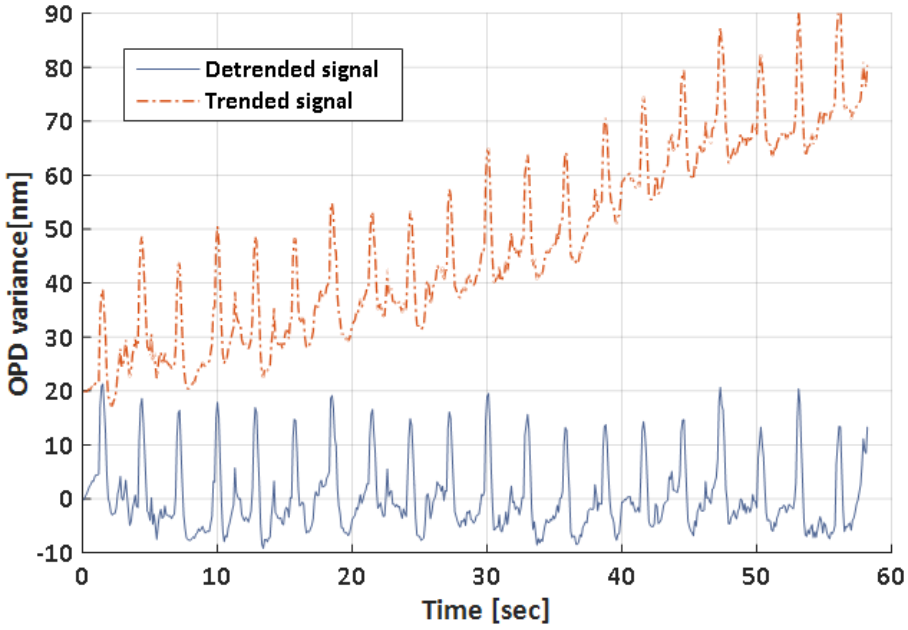

Figure 4.4: A trended cardiomyocyte signal and the de-trended signal.

The next change is that there are samples in which an increasing trend in OPD_h signal is observed (probably due to a drift during imaging of cardiomyocytes, see Fig.4, dash-dot line). The trended signal can falsify the positive and negative peak detection step. The reason is that we used first-order derivation to find peaks and after it we utilized Otsu's [92] thresholding method to find a proper threshold for positive and negative peaks. Therefore, finding a proper threshold in a trended signal is not possible. To de-trend the signal an approach similar to de-trending electro cardiogram signal has been utilized. The trended signal is de-trended by subtracting it from the fitted polynomial of degree six (See Fig.4.4, solid line). Fitted polynomial with degree of 6 is described with the following equation:

$$f(x) = \sum_{i=1}^{i=7} b_i x^{7-i} \quad (4)$$

Where "x"s are the sample points on each beating period and "b_i"s are the coefficient of

polynomial obtained with least-square criterion.

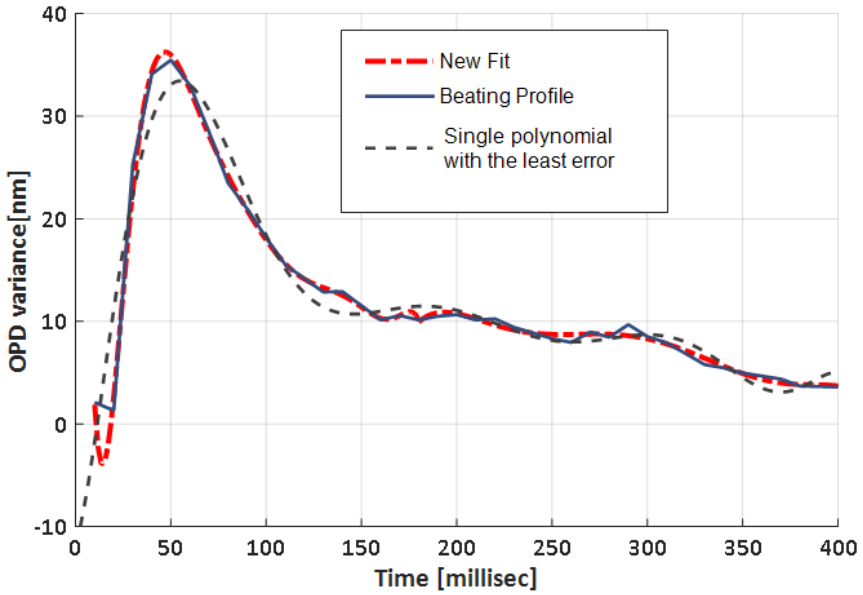

Figure 4.5: A single beat profile and the new fitting approach versus single polynomial approach.

Finally, each beating waveform should be fitted with a polynomial to analyze the physiology of the beating signal. This can help studying the effects of drugs on cardiac action potential. To find QRS complex of an ECG signal different methods are proposed [93-96]. For example, Christov. et.al [95] suggested peak finding and thresholding to detect *R* peaks. In this work, we tried several fitting approaches. In the previous work it has been mentioned that a polynomial with degree of 9 can fit the signal [42]. Also, in analyzing electrocardiogram signals polynomial with different degrees can be used. However, we realized that for the low beat-rate samples the waveform cannot be fitted with only a single polynomial (see Fig. 4.5). The reason is that the rising and falling time are different and it makes the rising-falling portion of the bating waveform appears asymmetrically. The variation is due to the presence of different ion channels and the mechanism by which they are sequentially activated during cardiac action potential [97]. The new fit consists of two fitting functions one for the rising-

falling portion and the other one for the flat region (resting time of the cells). The fitting function for the rising-falling section is a weighted polynomial with the degree of 9 and the shoulder section is a 6^{th} degree polynomial. The weights are assigned manually to get the best fit for the rising-falling section.

TABLE 4.1: Description of the cardiomyocyte dynamic parameters

Parameter	Description
Rising time	The time difference between Amp20 to Amp80(T_3-T_1)
Falling time	The time difference between Amp80 to Amp20(T_6-T_4)
IDB50	The time difference between two Amp50 (T_5-T_2)
Rising Slope	The amplitude difference at (T_3,T_1)
Falling Slope	The amplitude difference at (T_6,T_4)
Beat Rate	The total number of positive peaks in 60 seconds
Amplitude	Value difference from maximum to minimum amplitude

With the fitted polynomials curves, the amplitude value defined in Table. 4.1 can be calculated as the maximum value minus the minimum value on the fitted curve. Thus, the corresponding times for 20%, 50% and 80% of the amplitude signal (see Fig. 4.6) can be computed by solving the fitted polynomial equation. Having the times, we can compute multiple parameters including, rising time, falling time, IBD50, rising and falling slope. Then, all of the above mentioned parameters are measured for each individual beating period and a population average and standard deviations are computed. The description of the parameters can be found in Table 4.1 [42]. These parameters are vital for the analysis of drug candidates' effects on cardiomyocytes.

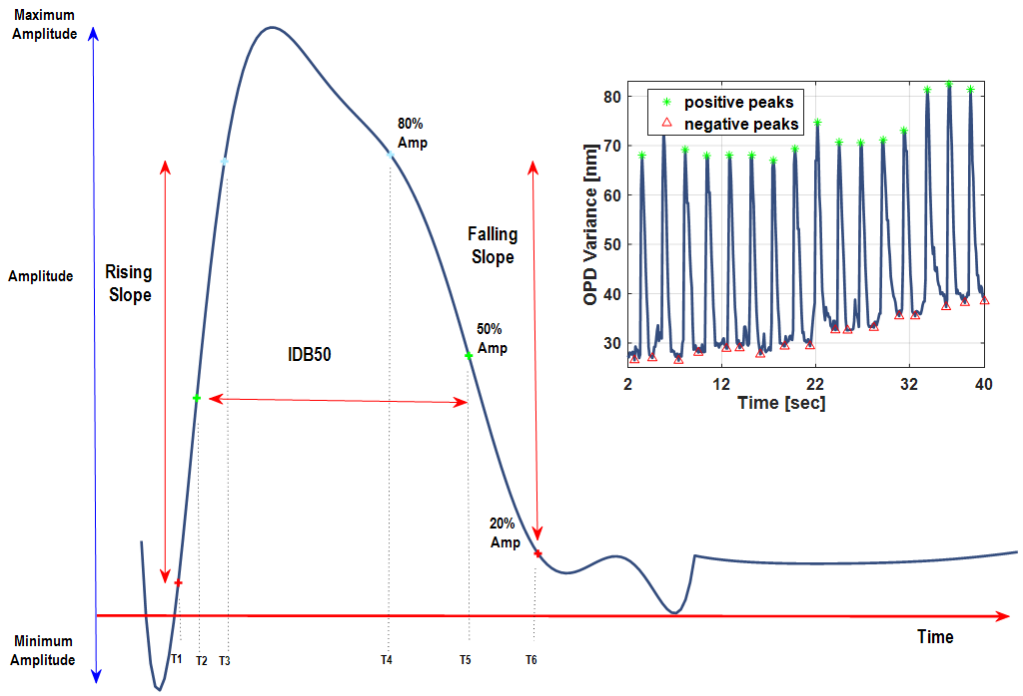

Figure 4.6: Representation of the fitted function on cardiac action potential and the definition of the multi-parameters

As it is mentioned above, the positive and negative peaks should be detected before the fitting step. Therefore, it requires finding positive and negative peaks by applying the first derivative technique to the beating signal. But, utilizing first derivative technique will provide so many unwanted peaks which should be removed. To do so, peaks between each positive and negative peak are removed.

d. Results and discussions

Having the fitted curves, all of the above mentioned parameters (Table.4.1) for each individual beating sample is measured. The parameters are evaluated according to the fitted

curve. Controlled OPD sequence in individual wells (*n=3* for each amount to drug) are recorded before addition of the drug, then E-4031 is added at different micromolar concentration in individual wells (in triplicate) and after a 15-min incubation period the OPD signal is again recorded in each of the treated wells. Table.4.2 shows the beat rate before and after treating the sample with E-4031. For each drug experiment three samples are provided. For each sample the number of positive peaks is considered as the beat rate. Beating profiles of the samples are presented in Fig.4.7.

Table 4.2: CARDIOMYOCYTE BEAT RATE BEFORE AND AFTER DRUG TREATMENT

Sample No#	Beat rate before treatment	Beat rate after treatment	Drug Amount (Micro Molar)
#1	**31**	**27**	**3 µM**
#2	**31**	**27**	**3 µM**
#3	**30**	**25**	**3 µM**
#4	28	23	10 µM
#5	29	23	10 µM
#6	29	23	10 µM
#7	**26**	**13**	**30 µM**
#8	**27**	**14**	**30 µM**
#9	**28**	**15**	**30 µM**
#10	27	11	100 µM
#11	27	11	100 µM
#12	26	12	100 µM

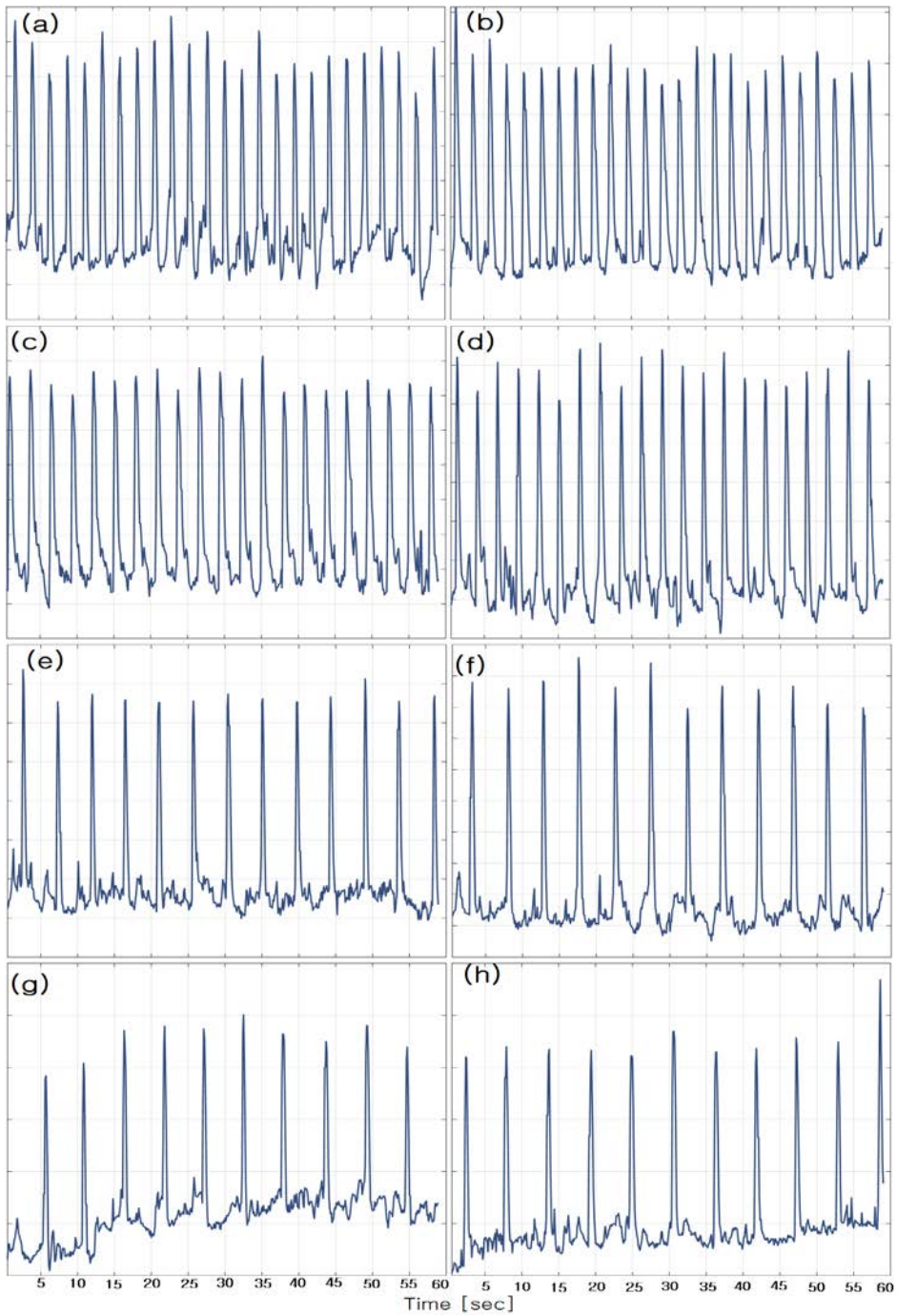

Figure 4.7: Two beating profiles for each drug treated samples; (a), (b) 3μM of E-4031; (c),(d) 10μM of E-4031;(e),(f) 30μM of E-4031 and (g),(h) 100μM of E-4031 is added.

Fig. 4.8 and 4.9 show the results of cardiomyocyte dynamic changes in response to different amount of drug. E-4031 is a synthetized class III antiarrhythmic toxin drug. E-4031 blocks the hERG-type potassium channels by binding to the open channels. This will reduce I_{kr} in cardiomyocytes which prolongs the QT-interval and thus change the cardiac action potential. According to the Fig.8, rising slope is always larger than the falling slope. This is also true for the controlled sample (Results not shown here). Also, according to the Fig. 9 rising time is shorter than falling time.

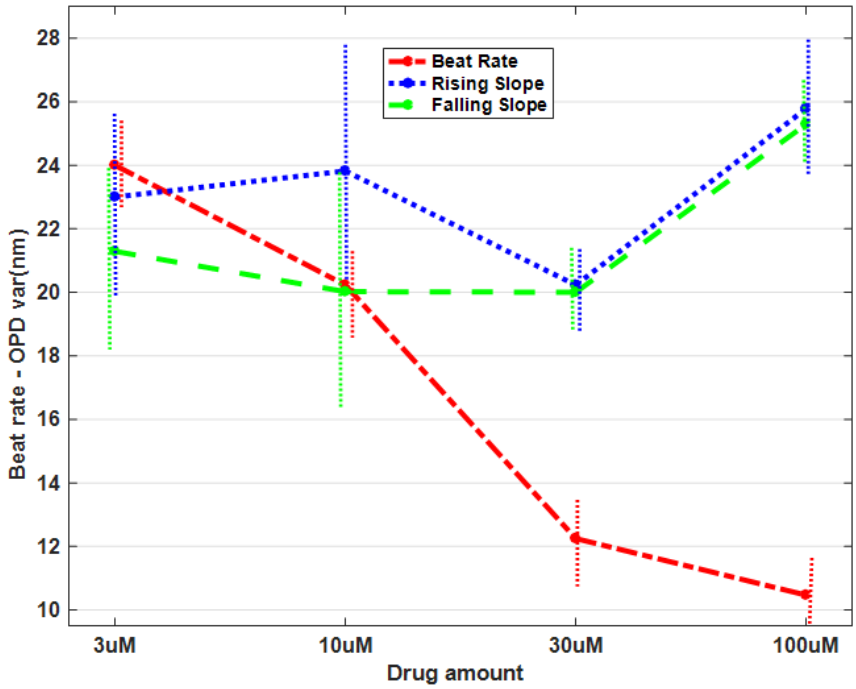

Figure 4.8: Beat rate, rising and falling slope in response to drug amount. Dotted lines are standard deviations.

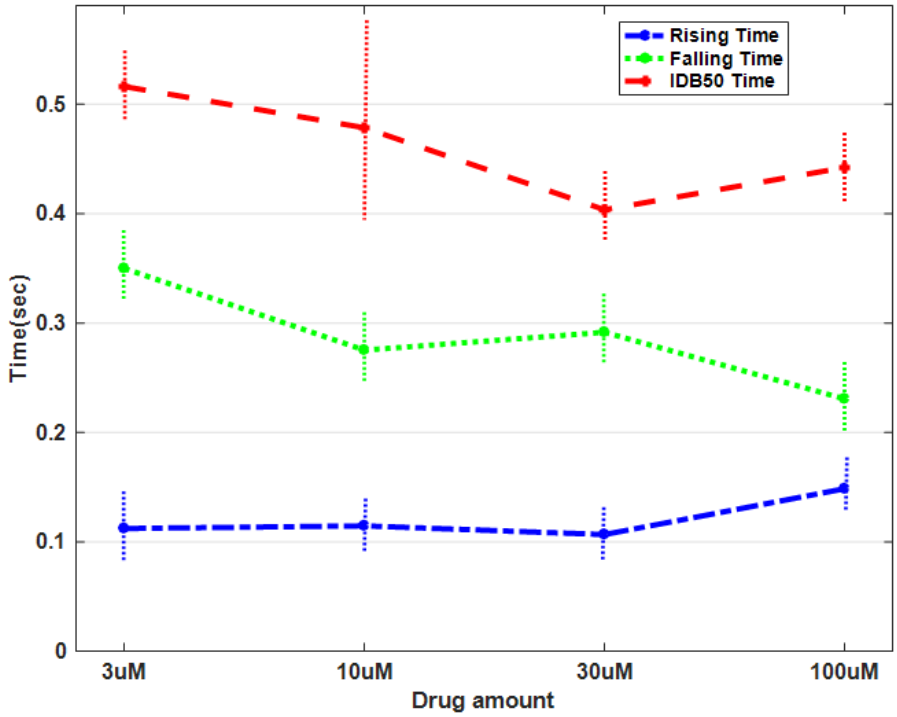

Figure 4.9: IDB50, rising and falling time in response to drug amount. Dotted lines are standard deviations.

e. Conclusion

In this section, we estimated physiologically relevant parameters of controlled and cardiomyocytes treated by different amount of E-4031 (class III antiarrhythmic drug) during the beating period. Our experimental results show that beat rate is decreasing while the amount of E-4031 is increasing. Indeed, IDB50, rising/falling slope and rising/falling time of the signal also changes with increasing amount of E-4031. We show that our method can be used to estimate different parameters related to cardiomyocytes in normal and drug-treated conditions and thus offer a useful tool for cardiotoxicity assessment in the drug development process.

5 Conclusion and Future Research Opportunities

The field of digital holographic microscopy (DHM) is very new and hot topic, and has so many opportunities for new and young researches. In this dissertation I wanted to show the application of DHM in life science studies and more specifically in red blood cell and cardiomyocytes. RBC can be considered as perfect phase object since it cannot be seen easily by normal optical devices unless we add stain or chemical dyes to the sample. Studying of heart cells treated by different amount of drugs is another interest of our group. It can be helpful for pharmacological interests and drug delivery purposes. The DHM application in life sciences is not limited only to RBC or heart muscle cells. It can be used in studying different cells for example muscle cells. In a new experiment we would like to see the quantitative difference between young skeleton muscle cells and old ones. Studying of different alcohols and the effects on RBC is another interest of our group. We would like to see the changes in the shape and morphology of RBC affected by the different type of alcohols. This is very important to measure the quantitative amount of damages alcohols can cause to RBC. In another experiment we would like to see the amount of RBC changes in different temperature condition. At different temperature we would like to measure the osmosis of RBC. It has been mentioned that RBC become more fragile in lower temperatures. Therefore the RBC membrane should break down quickly and number of ghost RBCs should increase significantly. Studying amount of expansion and shrinkage or RBC at different solutions is another important issues and we would like to study it in the future.

6 References

[1] Myung K. Kim Digital Holographic Microscopy Principles, Techniques, and Applications (page 153)

[2] J. Goodman and R. Lawrence, “Digital image formation from electronically detected holograms,” Appl. Phys. Lett. vol. 11, no. 77, 77–79 (1967).

[3] D. Carl, B. Kemper, G. Wernicke, and G. von Bally, “Parameter-optimized digital holographic microscope for high-resolution living-cell analysis,” Appl. Opt. vol. 43, no. 36, 6536–6544 (2004).

[4] C. Wagner, W. Osten, and S. Seebacher, “Direct shape measurement by digital wavefront reconstruction and multi-wavelength contouring,” Opt. Eng. Vol. 39, no.1, pp. 79–85 (2000).

[5] Y. Frauel, T. Naughton, O. Matoba, E. Tajahuerce, and B. Javidi, “Three-dimensional imaging and processing using computational holographic imaging,” Proc. IEEE vol. 94, pp. 636–653 (2006).

[6] F. Merola, L. Miccio, P. Memmolo, G. Caprio, A. Galli, R. Puglisi, D. Balduzzi, G. Coppola, P. Netti, and P. Ferraro, “Digital holography as a method for 3D imaging and estimating the biovolume of motile cells,” Lab Chip, vol. 13, pp. 4512–4516 (2013).

[7] I. Moon, M. Daneshpanah, B. Javidi, and A. Stern, “Automated three dimensional identification and tracking of micro/nano biological organisms by computational holographic microscopy,” Proc. IEEE 97, pp. 990–1010 (2009).

[8] F. Dubois, C. Yourassowsky, O. Monnom, J. Legros, O. Debeir, and P. Ham, “Digital holographic microscopy for the three-dimensional dynamic analysis of in vitro cancer cell migration,” J. Biomed. Opt. vol. 11, no. 5, 054032 (2006).

[9] D. Carl, B. Kemper, G. Wernicke, and G. von Bally, “Parameter-optimized digital holographic microscope for high-resolution living-cell analysis,” Appl. Opt. 43, 6536-6544 (2004).

[10] F. Merola, L. Miccio, P. Memmolo, G. Caprio, A. Galli, R. Puglisi, D. Balduzzi, G. Coppola, P. Netti, and P. Ferraro, “Digital holography as a method for 3D imaging and estimating the biovolume of motile cells,” Lab Chip 13, 4512-4516 (2013).

[11] F. Yi, I. Moon, and B. Javidi, “Cell morphology-based classification of red blood cells using holographic imaging informatics,” Biomedical Optics Express, 7, 2385-2399 (2016).

[12] B. Javidi, I. Moon, S. Yeom, and E. Carapezza, “Three-dimensional imaging and recognition of microorganism using single-exposure on-line (SEOL) digital holography,” Opt.Express. 13, 4492–4506 (2005).

[13] I. Moon, A. Anand, M. Cruz, and B. Javidi, “Identification of Malaria Infected Red Blood Cells via Digital Shearing Interferometry and Statistical Inference,” IEEE Photon. J . 5, 6900207-1 - 6900207-7 (2013).

[14] I. Moon and B. Javidi, “3D visualization and identification of biological microorganisms using partially temporal incoherent light in-line computational holographic imaging,” IEEE Trans. Med. Imag. 27, 1782–1790 (2008).

[15] F. Dubois, C. Yourassowsky, O. Monnom, J. Legros, O. Debeir, and P. Ham, “Digital holographic microscopy for the three-dimensional dynamic analysis of in vitro cancer cell migration,” J. Biomed. Opt. 11, 054032 (2006).

[16] K. Alm, H. Cirenajwis, L. Gisselsson, A. Wingren, B. Janicke, A. Molder, S. Oredsson, and J. Persson, Digital holography and cell studies (In Tech., 2011).

[17] B. Rappaz, F. Charriere, C. Depeursinge, P. Magistretti, and P. Marquet, “Simultaneous cell morphometry and refractive index measurement with dual-wavelength digital holographic microscopy and dye-enhanced dispersion of perfusion medium,” Opt. Lett. 33, 744-746 (2008).

[18] I. Moon and B. Javidi, “3D identification of stem cells by computational holographic imaging,” J. Roy. Soc. Interface. 4, 305–313 (2007).

[19] P. Marquet, B. Rappaz, P. Magistretti, E. Cuche, Y. Emery, T. Colomb, and C. Depeursinge, “Digital holographic microscopy: a noninvasive contrast imaging technique allowing quantitative visualization of living cells with sub wavelength axial accuracy,” Opt. Lett. 30, 468-470 (2005).

[20] B. Rappaz, E. Cano, T. Colomb, J. Kuhn, C. Depeursinge, V. Simanis, P. Magistretti, and P. Marquet, “Noninvasive characterization of the fission yeast cell cycle by monitoring dry mass with digital holographic microscopy,” J. Biomed. Opt. 14, 034049 (2009).

[21] B. Rappaz, I. Moon, F. Yi, B. Javidi, P. Marquet and G. Turcatti, “Automated multi-parameter measurement of cardiomyocytes dynamics with digital holographic microscopy” Opt. Express 23, 13333-13347 (2015).

[22] I. Moon, F. Yi, Y. Lee, B. Javid, D. Boss, and P. Marquet, “Automated quantitative analysis of 3D morphology and mean corpuscular hemoglobin in human red blood cells stored in different periods,” Opt. Express 21, 30947-30957 (2013).

[23] K. Jaferzadeh and I. Moon, “Quantitative investigation of red blood cell three-dimensional geometric and chemical changes in the storage lesion using digital holographic microscopy,” J. Biomed. Opt. 20, 111218 (2015).

[24] B. Rappaz, A. Barbul, Y. Emery, R. Korenstein, C. Depeursinge, P. Magistretti, and P. Marquet, “Comparative study of human erythrocytes by digital holographic microscopy, confocal microscopy, and impedance volume analyzer,” Cytometry A 73, 895-903 (2008).

[25] K. Jaferzadeh and I. Moon, “Human red blood cell recognition enhancement with three-dimensional morphological features obtained by digital holographic imaging,” J. Biomed. Opt. 21, 126015 (2016).

[26] I. Moon, F. Yi and B. Rappaz, “Automated tracking of temporal displacements of a red blood cell obtained by time-lapse digital holographic microscopy.” Appl. Opt. 55, A86-A94 (2016).

[27] F. Yi , I. Moon and Y. H. Lee, “Three-dimensional counting of morphologically normal human red blood cells via digital holographic microscopy.” J. Biomed. Opt. 20, 016005 (2015).

[28] P. Marquet, B. Rappaz, P. J. Magistretti, E. Cuche, Y. Emery, T. Colomb, and C. Depeursinge, “Digital Holographic Microscopy: a Noninvasive Contrast Imaging Technique Allowing Quantitative Visualization Of Living Cells With Sub Wavelength Axial Accuracy,” Opt. Lett., 30(5), 468-470 (2005).

[29] E. Cuche, P. Marquet, and C. Depeursinge, “Simultaneous amplitude and quantitative phase contrast microscopy by numerical reconstruction of Fresnel off-axis holograms,” Appl. Opt. 38, 6994-7001 (1999).

[30] T. Colomb, E. Cuche, F. Chariere, J. Kuhn, N. Aspert, P. Marquet, and C. Depeursinge, “Automatic procedure for aberration compensation in digital holographic microscopy and application to specimen shape compensation,” Appl. Opt. 45,851-863 (2006).

[31] P.B. Canham, “The minimum energy of bending as a possible explanation of the biconcave shape of the human red blood cell,” Journal of Theoretical Biology, 26, 61-81 (1970).

[32] C. Uzoigwe, “The human erythrocyte has developed the biconcave disc shape to optimise the flow properties of the blood in the large vessels,” Medical Hypotheses, 67, 1159-1163 (2006).

[33] Z. Tu, “Geometry of membranes,” Journal of Geometry and Symmetry in Physics, 24, 45-75 (2011).

[34] M. Bessis, R. Weed, and P. Leblond, Red Cell Shape, Physiology, Pathology Ultrastructure, (Springer, 2012).

[35] Y. Kim, H. Shim, K. Kim, H. Park, S. Jang, and Y. Park, “Profiling individual human red blood cells using common-path diffraction optical tomography,” Scientific Reports, 4, 6659 (2014).

[36] C. Aubron, A. Nichol, D. Cooper, and R. Bellomo, “Age of red blood cells and transfusion in critically ill patients,” Annals of Intensive Care, 3, 1-11 (2013).

[37] D. Triulzi and M. Yazer, “Clinical studies of the effect of blood storage on patient outcomes,” Transfus. Apheresis Sci., 43, 95-106 (2010).

[38] G. Bosman, J. Werre, F. Willekens, V. Novotny, “Erythrocyte ageing in vivo and in vitro: structural aspects and implications for transfusion,” Transfus Med., 18, 335-347 (2008).

[39] Y. Park, C. Best, T. Auth, N. Gov, S. Safran, G. Popescu, and M. Feld, “Metabolic remodeling of the human red blood cell membrane,” Proceedings of the National Academy of Sciences, 107, 1289-1294 (2010).

[40] M. Buttarello and M. Plebani, “Automated blood cell counts,” American Journal of Clinical Pathology,” 130, 104-116 (2008).

[41] T. S. Natan, et. Al, "Whole-cell-analysis of live cardiomyocytes using wide-field interferometric phase microscopy." Biomed. Opt. Express, vol. 1, no. 2, pp. 706-719 (2010).

[42] B. Rappaz, et.al “Automated multi-parameter measurement of cardiomyocytes dynamics with digital holographic microscopy”. Optics express, vol. 23, no. 10, pp. 13333-13347(2015).

[43] Biao Xi, et.al “Functional Cardiotoxicity Profiling and Screening Using the xCELLigence RTCA Cardio System”, J Lab Autom, vol. 16, no. 6, pp. 415–421 (2011).

[44] D. Gabor, “A new microscope principle,” Nature 161, 777–778 (1948).

[45] D. Gabor, “Microscopy by reconstructed wavefronts,” Proc. Roy. Soc. A197, 454–487 (1949).

[46] D. Gabor, “Microscopy by reconstructed wavefronts: II,” Proc. Phys. Soc. B64, 449–469 (1951).

[47] “Introduction to Modern Digital Holography With Matlab”

[48] https://en.wikipedia.org/wiki/Red_blood_cell

[49] R. Barer, “Determination of dry mass, thickness, solid and water concentration in living cells,” Nature, vol. 172, no. 4389, pp. 1097–1098 (1953).

[50] J. Kato, Gregory. “Understanding the Erythrocyte Storage Lesion.” Anesthesiology 117.6 (2012): 1159–1161. PMC. Web. 28 Sept. 2017.

[51] R.T. Card, “Red cell membrane changes during storage.” Transfus Med Rev. 1988 Mar;2(1):40-7.

[52] Kor DJ., Van Buskirk CM, Gajic O. “Red Blood Cell Storage Lesion.” Bosn J Basic Med Sci. 2009 Oct;9 Suppl 1:21-7.

[53] Joanna F. Flatt, Waleed M. Bawazir and Lesley J. Bruce “The involvement of cation leaks in the storage lesion of red blood cells.” Front Physiol. 2014; 5: 214. doi: 10.3389/fphys.2014.00214.

[54] P.B. Canham and A. Burton, “Distribution of Size and Shape in Populations of Normal Human Red Cells,” Circ Res., 22(3), 405-422 (1968).

[55] K. Tachev, K. Danov, and P. Kralchevsky, “On the mechanism of stomatocyte-echinocyte transformations of red blood cells: experiment and theoretical model,” Colloids and Surfaces B: Biointerfaces, 34(2), 123-140 (2004).

[56] X. Long, J.Fang, L.Yao, Q.Xiao, T.Pan, “Correlation Analysis between Mean Corpuscular Hemoglobin and Mean Corpuscular Volume for Thalassemia Screening in Large Population.” American Journal of Analytical Chemistry, 2014, 5, 901-907.

[57] GM. Rao, L. Morghom, S. Mansori. “Negative Correlation between Erythrocyte Count and Mean Corpuscular Volume or Mean Corpuscular Haemoglobin in Diabetic and Non-Diabetic Subjects.” Horm Metab Res. 1985 Oct;17(10):540-1.

[58] Y. Yawata, Cell Membrane: The Red Blood Cell as a Model (Wiley-VCH Verlag, 2004).

[59] D. Surgenor, The Red Blood Cell (Academic Press, 2013).

[60] S. Robinson, C. Janssen, E. Fretz, B. Berry, A. Chase, A. Siega, R. Carere, A. Fung, G. Simkus, W. Klinke, and J. Hilton. “Red Blood Cell Storage Duration and Mortality in Patients Undergoing Percutaneous Coronary Intervention,” Am Heart J., 159(5), 876-881 (2010).

[61] R. Marabini and J. Carazo “Pattern recognition and classification of images of biological macromolecules using artificial neural networks,” Biophysical Journal, 66, 1804-1814 (1994).

[62] A. Khashman, “IBCIS: Intelligent blood cell identification system,” Progress in Natural Science, 18, 1309-1314 (2008).

[63] M. Veluchamy, K. Perumal, and T. Ponuchamy, “Feature extraction and classification of blood cells using artificial neural network,” American Journal of Applied Sciences, 9, 615-619 (2012).

[64] J. Bacus and J. Weens, “An automated method of differential red blood cell classification with application to the diagnostics of anemia,” Journal of Histochemistry & Cytochemistry, 25, 614-632 (1977).

[65] L. Wheeless, R. Robinson, O. Lapets, C. Cox, A. Rubio, M. Weintraub, and L. Benjamin, “Classification of Red Blood Cells as Normal, Sickle, or Other Abnormal, Using a Single Image Analysis Feature,” Cytometry, 17, 159-166 (1994).

[66] P. Rakshita and K. Bhowmik “Detection of Abnormal Findings in Human RBC in Diagnosing Sickle Cell Anaemia Using Image Processing,” Procedia Technology, 10, 28-36 (2013).

[67] H. Lee and Y. Chen, “Cell morphology based classification for red cells in blood smear images,” Pattern Recognition Letters, 49, 155-161 (2014).

[68] C. Koch, L. Li, D. Sessler, P. Figueroa, G. Hoeltge, T. Mihaljevic, and E. Blackstone, “Duration of red-cell storage and complications after cardiac surgery,” New England Journal of Medicine, 358, 1229-1239 (2008).

[69] F. Yi, I. Moon, B. Javidi, D. Boss, and P. Marquet, “Automated segmentation of multiple red blood cells with digital holographic microscopy,” Journal of Biomedical Optics, 18, 026006 (2013).

[70] G. Forman, “An extensive empirical study of feature selection metrics for text classification,” Journal of Machine Learning Research, 3, 1289-1305 (2003).

[71] Y. Bengio and Y. Grandvalet, “No unbiased estimator of the variance of K-fold cross-validation,” Journal of Machine Learning Research, 5, 1089-1105 (2004).

[72] J. David and C. MacKay, “Bayesian Interpolation,” Neural Computation, 4, 415-447 (1992).

[73] J. Dykens and Y. Yawata, Cell Membrane (Wiley, 2003).

[74] H. Strey, M. Peterson, and E. Sackmann, “Measurement of erythrocyte membrane elasticity by flicker eigenmode decomposition,” Biophys. J. 69, 478-488 (1995).

[75] B. Bhaduri, M. Kandel, C. Brugnara, K. Tangella, and G. Popescu, “Optical assay of erythrocyte function in banked blood,” Sci. Rep. 4, 6211 (2014).

[76] B. Rappaz, A. Barbul, A. Hoffmann, D. Boss, R. Korenstein, C. Depeursinge, P. Magistretti, and P. Marquet, “Spatial analysis of erythrocyte membrane fluctuations by digital holographic microscopy,” Blood Cells Mol. Dis. 42 228-232 (2009).

[77] J. Laurie, D. Wyncoll, and C. Harrison, “New versus old blood - the debate continues,” Crit. Care 14, 130 (2010).

[78] A. Alessandro, G. Liumbruno, G. Grazzini, and L. Zolla, “Red blood cell storage: the story so far,” Blood Transfus 8, 82-88 (2010).

[79] J. Cluitmans, V. Chokkalingam, A. Janssen, R. Brock, W. Huck, and G. Bosman, “Alterations in red blood cell deformability during storage: a microfluidic approach,” Biomed Res. Int. 764268 (2014).

[80] H. Park, S. Lee, M. Ji, K. Kim, Y. Sohn, S. Jang and Y. Park, “Measuring cell surface area and deformability of individual human red blood cells over blood storage using quantitative phase imaging,” Sci. Rep. 6, 34257 (2016).

[81] I. Safeukui, et al. “Quantitative assessment of sensing and sequestration of spherocytic erythrocytes by the human spleen,” Blood. 120, 424–430 (2012).

[82] S. M. Frank, et al. “Decreased erythrocyte deformability after transfusion and the effects of erythrocyte storage duration,” Anesth Analg. 116, 975–981 (2013).

[83] M. Bardyn, B. Rappaz, K. Jaferzadeh, D. Crettaz, J. Tissot, I. Moon, G. Turcatti, N. Lion, and M. Prudent, “Red blood cells aging markers, a multi-parametric analysis,” Blood Transfus.15, 239-248(2017)..

[84] C. A. Schneider, W. S. Rasband and K. W. Eliceiri, "NIH Image to ImageJ: 25 years of image analysis", Nat. Methods. 9: 671-675 (2012).

[85] P. Thévenaz, U.E. Ruttimann and M. Unser, "A Pyramid Approach to Subpixel Registration Based on Intensity," IEEE Trans. Image Process. 7, 27-41 (1998).

[86] J. Evans, W. Gratzer, N. Mohandas, K. Parker and J. Sleep, “Fluctuations of the red blood cell membrane: relation to mechanical properties and lack of ATP dependence,” Biophys. J. 94, 4134-4144 (2008).

[87] Y. Park, C. Best, K. Badizadegan, R. Dasari, M. Feld, T. Kuriabova, M. Henle, A. Levine, and G. Popescu, “Measurement of red blood cell mechanics during morphological changes,” Proc. Natl. Acad. Sci. 107, 6731-6736 (2010).

[88] G. Marcelli, K. Parker, and C. Winlove, “Thermal fluctuations of red blood cell membrane via a constant-area particle-dynamics model,” Biophys. J. 89, 2473-2480 (2005).

[89] O. Rubin, G. Canellini, G., J. Delobel, N. Lion, and J.D. Tissot “Red Blood Cell Microparticles: Clinical Relevance.” Transfus Med Hemother. 39, 342–347 (2012).

[90] N. Gov and S. Safaran, “Red blood cell membrane fluctuations and shape controlled by ATP-induced cytoskeletal defects,” Biophys. J. 88 1859-1874 (2005).

[91] M. Prudent, et al, “Loss of Protein Tyr-phosphorylation During in vitro Storage of Human Erythrocytes: Impact on RBC Morphology.” Transfusion. 54, 49A–50A (2014).